Photochemical Evolution of the 2013 California Rim Fire: Synergistic Impacts of Reactive Hydrocarbons and Enhanced Oxidants

Glenn M. Wolfe[1], Thomas F. Hanisco[1], Heather L. Arkinson[2], Donald R. Blake[3], Armin Wisthaler[4,5], Tomas Mikoviny[5], Thomas B. Ryerson[6,7,*], Ilana Pollack[7,**], Jeff Peischl[7], Paul O. Wennberg[8,9], John D. Crounse[8], Jason M. St. Clair[8,***], Alex Teng[8,****], L. Gregory Huey[10], Xiaoxi Liu[10,*****], Alan Fried[11], Petter Weibring[11], Dirk Richter[11], James Walega[11], Samuel R. Hall[12], Kirk Ullmann[12], Jose L. Jimenez[7,13], Pedro Campuzano-Jost[7,13], T. Paul Bui[14], Glenn Diskin[15], James R. Podolske[14], Glen Sachse[15,16,†], and Ronald C. Cohen[17,18]

[1]Atmospheric Chemistry and Dynamics Laboratory, NASA Goddard Space Flight Center, Greenbelt, MD, USA
[2]Department of Oceanic and Atmospheric Science, University of Maryland, College Park, MD, USA
[3]Department of Chemistry, University of California Irvine, Irvine, CA, USA
[4]Institute for Ion Physics and Applied Physics, University of Innsbruck, Innsbruck, Austria
[5]Department of Chemistry, University of Oslo, Oslo, Norway
[6]Chemical Sciences Laboratory, NOAA, Boulder, CO, USA
[7]Cooperative Institute for Research in Environmental Sciences, University of Colorado Boulder, Boulder, CO, USA
[8]Division of Geological and Planetary Sciences, California Institute of Technology, Pasadena, CA, USA
[9]Division of Engineering and Applied Science, California Institute of Technology, Pasadena, CA, USA
[10]School of Earth and Atmospheric Sciences, Georgia Institute of Technology, Atlanta, GA, USA
[11]Institute of Arctic and Alpine Research, University of Colorado, Boulder, CO, USA
[12]Atmospheric Chemistry Observations and Modeling Laboratory, National Center for Atmospheric Research, Boulder, CO, USA
[13]Department of Chemistry, University of Colorado Boulder, Boulder, CO, USA
[14]Atmsopheric Sciences Branch, NASA Ames Research Center, Moffett Field, CA, USA
[15]NASA Langley Research Center, Hampton, VA, USA
[16]National Institute of Aerospace, Hampton, VA, USA
[17]Department of Earth and Planetary Sciences, University of California, Berkeley, CA, USA
[18]College of Chemistry, University of California, Berkeley, CA, USA
*Now at Scientific Aviation, Boulder, CO, USA
**Now at Department of Atmospheric Science, Colorado State University, Fort Collins, CO, USA
***Now at Joint Center for Earth Systems Technology, University of Maryland Baltimore County, Baltimore, MD, USA
****Now at Fifty Years, San Francisco, CA, USA
*****Now at California Air Resource Board, Los Angeles, CA, USA
†Deceased

Correspondence to: Glenn M. Wolfe (glenn.m.wolfe@nasa.gov)

Abstract

Large wildfires markedly alter regional atmospheric composition, but chemical complexity challenges model predictions of downwind impacts. Here, we elucidate key facets of gas-phase photochemistry and assess novel chemical processes via a case study of the 2013 California Rim Fire plume. Airborne in situ observations, acquired during the NASA Studies of Emissions, Atmospheric Composition, Clouds and Climate Coupling by Regional Surveys (SEAC^{4}RS) mission, illustrate the evolution of

40 volatile organic compounds (VOC), oxidants, and reactive nitrogen over 12 hours of atmospheric aging. Measurements show rapid formation of ozone and peroxyacyl nitrates (PNs), sustained peroxide production, and prolonged enhancements in oxygenated VOC and nitrogen oxides (NO_x).

Measurements and Lagrangian trajectories constrain a 0-D puff model that approximates plume photochemical history and provides a framework for evaluating key processes. Simulations examine the effects of 1) previously-unmeasured

45 reactive VOC identified in recent laboratory studies, and 2) emissions and secondary production of nitrous acid (HONO). Inclusion of estimated unmeasured VOC leads to a 250% increase in OH reactivity and a 70% increase in radical production via oxygenated VOC photolysis. HONO amplifies radical cycling and serves as a downwind NO_x source, although two different HONO production mechanisms (particulate nitrate photolysis and heterogeneous NO_2 conversion) exhibit markedly different effects on ozone, NO_x, and PNs. Analysis of radical initiation rates suggests that oxygenated VOC photolysis is a

50 major radical source, exceeding HONO photolysis when averaged over the first 2 hours of aging. Ozone production chemistry transitions from VOC-sensitive to NO_x-sensitive within the first hour of plume aging, with both peroxide and organic nitrate formation contributing significantly to radical termination. To simulate smoke plume chemistry accurately, models should simultaneously account for the full reactive VOC pool and all relevant oxidant sources.

1 Introduction

55 Biomass burning accounts for at least 30% of global emissions of non-methane volatile organic compounds (VOC) (Akagi et al., 2011; Andreae, 2019; Yokelson et al., 2008). Pyrogenic VOC fuel the production of ozone and secondary organic aerosol, with significant consequences for regional and global air quality and climate (Jaffe and Wigder, 2012; McClure and Jaffe, 2018; Buysse et al., 2019; Val Martin et al., 2015; Hodshire et al., 2019). Pyrogenic emissions consist of thousands of unique compounds. Existing emission inventories include over 100 individual VOC (Andreae, 2019; Akagi et al., 2011). These

60 compilations are incomplete, and it is estimated that previously "unidentified" VOC account for ~50% of total pyrogenic VOC mass (Akagi et al., 2011; Yokelson et al., 2013; Gilman et al., 2015). Recent advances in instrumentation have broadened the suite of detectable VOC to over 500 species (Sekimoto et al., 2018; Hatch et al., 2019, 2017; Koss et al., 2018), although significant uncertainty remains regarding the speciation, reactivity, and fate of this extended VOC pool.

The photochemistry of biomass burning plumes is perhaps less well understood than emissions, especially within the

65 context of total reactive VOC. Reported observations of ambient smoke typically encompass a few hours of physical age and include a (relatively) limited set of compounds (Akagi et al., 2012, 2013; Alvarado et al., 2010; Liu et al., 2016; Müller et al., 2016). Detailed simulations may provide some insight into the chemistry of unidentified VOC, though models are often under-constrained and both model and measurement uncertainties can be large (Lonsdale et al., 2019; Alvarado et al., 2015; Müller et al., 2016; Mason et al., 2001; Liu et al., 2016). With extended VOC inventories from recent laboratory work (Hatch et al.,

70 2017; Koss et al., 2018), several studies have begun characterizing the impacts of previously unidentified VOC. Analyzing a series of laboratory burns, Coggon et al. (2019) estimate that species included in the Master Chemical Mechanism

(MCMv3.3.1) account for ~60% of the primary hydroxyl radical (OH) reactivity measured via Proton Transfer Time-of-flight Mass Spectrometry (PTR-MS). This study also demonstrates that furans, a previously unconsidered class of reactive VOC, may increase O_3 production within an agricultural fire plume by ~10% over the first hour of aging. Decker et al. (2019) estimate

75 that the MCM accounts for ~30% of the observed nitrate radical (NO_3) reactivity in the same laboratory experiments.

Despite improved knowledge of pyrogenic VOC speciation, it remains unclear how to best synthesize this information within existing regional/global model frameworks. It is not feasible to add a multitude of new species to chemical mechanisms; indeed, many global models do not explicitly account for all "known" VOC, let alone the large fraction of unidentified VOC (Duncan et al., 2007; Wiedinmyer et al., 2011). Nor is it evident that such modifications would improve model results, as

80 plume chemistry may be a "sub-grid scale" process more suited to parameterization than explicit simulation. On the other hand, reactive VOC chemistry can persist for days downwind of a fire (Mauzerall et al., 1998; Alvarado et al., 2020; Forrister et al., 2015), and an improved representation of such processes may alter regional budgets of ozone, CO, oxidized VOC, reactive nitrogen, and organic aerosol.

Oxidant sources also remain poorly understood in this environment. Smoke plumes are photochemically complex due to

85 spatial and temporal variability in radical precursors, radiation, and other factors (Wang et al., 2021). Recent work has highlighted the importance of nitrous acid (HONO) emissions as a radical source in nascent smoke plumes (Peng et al., 2020; Theys et al., 2020; Robinson et al., 2021). Secondary HONO production via heterogeneous processes may sustain downwind radical production in some, but not all, smoke plumes (Alvarado and Prinn, 2009; Alvarado et al., 2015). Multiple mechanisms have been proposed to explain observed HONO in other environments (Zhang et al., 2019), but their controlling factors and

90 potential impacts are not well-characterized.

Here, we utilize a case study of the 2013 California Rim Fire to examine the impacts of newly identified reactive VOC and HONO on gas-phase chemistry. Airborne in situ observations from the NASA Studies of Emissions, Atmospheric Composition, Clouds and Climate Coupling by Regional Surveys (SEAC⁴RS) mission constrain the evolution of oxidants and oxidation products over ~12 hours of atmospheric aging. We combine these observations with air mass trajectories to drive a

95 0-D puff model that approximates plume aging. With this framework, we illustrate how an extended VOC pool and various HONO sources alter the chemistry of oxidants, oxidized VOC, reactive nitrogen, and ozone. We evaluate model results through comparison with observations and use the model to quantify time and mechanism-dependent changes in OH reactivity, radical production/termination, and ozone production sensitivity to VOC and NO_x.

2 Methods

100 ### 2.1 Rim Fire and SEAC⁴RS

The Rim Fire was an extreme wildfire in the central Sierra Nevada Mountains of California (37.85°N, 120.08°W). Ignited by an illegal campfire on 17 August 2013, the fire was not fully contained until 24 October 2013 and consumed a total area exceeding 1000 km². At the time of SEAC⁴RS flights, the fire front spanned a width of ~40 km in both the N-S and E-W

directions. Fuels consisted mostly of mixed conifer forest (Lydersen et al., 2014). Previous Rim Fire studies have investigated

105 fire meteorology (Peterson et al., 2015), emissions (Liu et al., 2017; Yates et al., 2016; Saide et al., 2015), aerosol properties
(Forrister et al., 2015; Adler et al., 2019; Perring et al., 2017), radiative effects (Yu et al., 2016a), and regional chemistry model
performance (Baker et al., 2018). We focus here on downwind gas-phase photochemistry.

   SEAC^{4}RS was a NASA-funded effort to characterize the processes controlling atmospheric properties in the summertime
U.S. (Toon et al., 2016). We utilize in situ observations acquired from the NASA DC-8 aircraft, which sampled Rim Fire

110 outflow on 26 and 27 August 2013. Analysis focuses on the "long-axis" portion of the 26 August flight, which extends from
directly over the fire to 470 km downwind (Fig. 1). The actual sample time window for this leg is UTC 23:06 to 23:57, and
the physical smoke age ranges from 0 to ~12 hours (Sect. 2.2). The aircraft maintained a pressure altitude of 4.3 km until 23:32
(smoke age ~5 h), when it descended to 3.6 km (Supplementary Information (SI) Fig. S1). Terrain was mountainous, and
corresponding altitude above ground level ranged from 1.3 to 3.2 km. Sampling was predominantly in the upper edge of the

115 smoke plume, which mostly resided in the lower free troposphere according to boundary layer depth derived from trajectory
meteorological fields (Fig. S1c). The modified combustion efficiency (MCE) near the source ranged from 0.91 to 0.94,
indicating a mix of flaming and smouldering combustion. While the DC-8 also sampled Rim Fire smoke as old as 2 – 3 days,
influence from other fires, surface-atmosphere exchange, and changing background concentrations complicates analysis of
that data.

120   SI Table S1 lists the instruments and measurement accuracy for observations used in this study; the payload is further
detailed in Toon et al. (2016). Fast (1 Hz) data are averaged to the 40-second collection window of the Whole Air Sampler
(WAS). Normalized excess mixing ratios (NEMRs) are calculated using carbon monoxide (CO) from the Differential
Absorption Carbon Monoxide Measurement (DACOM) as the dilution tracer.

$$NEMR(X) = \Delta X/\Delta CO = (X - X_b)/(CO - CO_b) \qquad (1)$$

125 Here, X is the observed mixing ratio and X_b is the background mixing ratio. Fast observations fluctuate rapidly in fire plumes
and can sometimes contain gaps over a portion of a WAS sampling interval. We adopt a custom averaging procedure to ensure
rigorous NEMR calculation for such data. First, each 1 Hz variable X is time-aligned to DACOM CO via optimized lag-
correlation. Second, CO is filtered to exclude points where X is missing. Finally, X and the filtered CO are averaged to the
WAS time base. Executing this procedure over all data effectively creates a unique, gap-filtered, WAS-averaged DACOM CO

130 for each variable. Background mixing ratios are averaged over a single WAS sample collected east of the plume (orange star
in Fig. 1). We also explored using observations just upwind of the fire for background estimation but found poor agreement
between the modelled and observed O$_3$ NEMR in this case due to higher upwind O$_3$ (78 vs. 50 ppbv). Figure S2 shows the
dilution factor as a function of plume age, which ranges from 1 to 24.
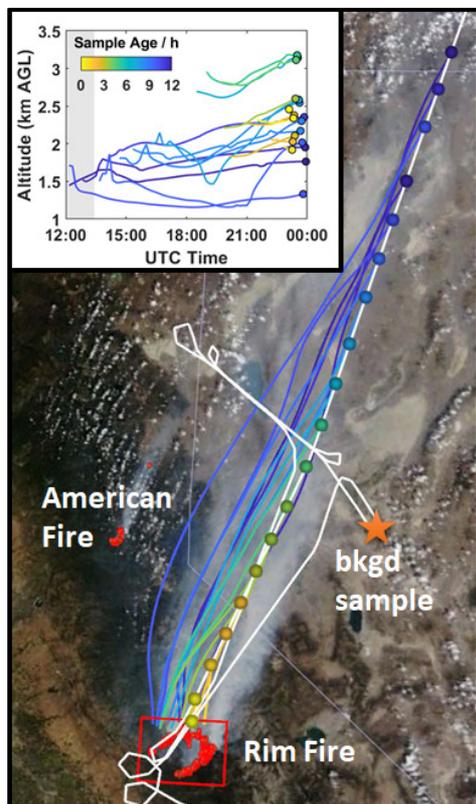
Figure 1. Map of the study region. The background shows visible imagery and fire counts (red dots) from Terra/MODIS (https://worldview.earthdata.nasa.gov/). The white line is the DC-8 flight track. The aircraft entered from the south, flew over the fire, proceeded NE to do a missed approach at Fallon airport (near orange star), executed a "wall" pattern of perpendicular transects at several altitudes, and returned to the fire before proceeding NE along the long axis leg. Colored circles denote WAS sample locations and colored lines are the corresponding median trajectories. Yellow-to-blue shading indicates Lagrangian plume age at the time of sampling (see color bar in inset). The orange star is the location of the background sample. The red box is the "Rim Fire" box used for trajectory filtering. (Inset) Time series of median trajectory altitudes with respect to ground level. Colored circles denote the observation time. Gray shaded area indicates night time.

2.2 Trajectory Analysis

Air mass trajectories provide an estimate of smoke age and inputs for the puff model described below. Trajectories are computed with the Hybrid Single-Particle Lagrangian Integrated Trajectory (HYSPLIT) Model (Stein et al., 2015), interfaced with custom MATLAB software for input and output handling (https://github.com/AirChem/HYSPLITcontrol, last accessed 1 Nov 2021). Trajectories are initialized at the midpoint of each WAS sample and run backward in time for 48 hours. Outputs include both position and meteorology (temperature, pressure, relative humidity, solar zenith angle (SZA), and boundary layer depth). To build statistics, we utilize archive meteorological fields from the North American Mesoscale Forecast System (NAMs, 12 km, 1-hour) and North American Regional Reanalysis (NARR, 32 km, 3-hour) datasets (https://ready.arl.noaa.gov/archives.php, last accessed 24 March 2020). Trajectories run as meteorological ensembles with HYSPLIT default settings (27 members, 1 grid-point horizontal shift, 0.01 sigma unit vertical shift), giving 54 trajectories per initialization. Next, we define a geographic box for the Rim Fire based on satellite imagery and fire counts (Fig. 1). Trajectories are filtered to exclude those not passing through this box. Filtered trajectories are spatially averaged using a geometric median,

resulting in one "median trajectory" for each observation (Fig. 1, inset). Meteorological quantities are averaged via arithmetic mean.

We define Lagrangian smoke age from the time when an averaged trajectory first intersected the Rim Fire box out to the
150 downwind time of sampling. The standard deviation of the smoke age from individual trajectories is typically ~9% of the mean for each ensemble, and we take this as a 1σ precision estimate. Smoke at our nominal starting point (the North end of the box) is actually a mixture of ages. Based on observed wind speed, we estimate a transit time of ~1 hour for emissions from the Southern-most fire front to reach the North end of the box. We take half of this value as an approximation for variability in actual smoke age. The total estimated uncertainty in average smoke age is then 9% + 0.5 h.

155 **2.3 Puff Model**

Simulation of any fire plume is challenging due to high concentrations, strong dilution, aerosol radiative perturbations, and other factors. SEAC[4]RS did not sample the core of the Rim Fire plume, and smoke ages of $0 - 12$ hours were probed over a single hour of flight. Thus, if we wish to compare with observations, it is not adequate to represent the Rim Fire as a single Lagrangian plume. Detailed fire plume models have improved in recent years (Lonsdale et al., 2019), but observational
160 constraints are limited compared to the complexity of such a model. The goal of our simulation is to obtain a meaningful comparison against observations without over-elaboration (Box, 1976).

In our model framework, the plume is approximated as a series of 0-dimensional "puffs." The puff model is developed within the Framework for 0-D Atmospheric Modelling (F0AMv4.2.1, available at https://github.com/AirChem/F0AM/) (Wolfe et al., 2016). One puff is simulated for each WAS sample/trajectory pair shown in Fig. 1. Each puff evolves in real
165 time along the "average trajectory" with meteorological constraints updated every 10 minutes. For each puff, along-trajectory pressure, temperature, relative humidity, and solar zenith angle are constrained with averaged trajectory output. Trajectory meteorology is rescaled by multiplicative factors (typically within a few percent of unity) based on the ratio of observed-to-trajectory values at trajectory endpoints. Photolysis frequencies are semi-constrained to observations using a two-part scaling that helps account for smoke radiative perturbations (Appendix A). Variations in scaling factors suggest stronger attenuation
170 in the UV than the visible (compare $J(O^1D)$ and $J(NO_2)$ in Fig. A1b). Chemical concentrations from the endpoint of each puff are extracted for comparison with observations.

Initial concentrations are the same for all puffs. These are estimated by combining Rim Fire emission ratios (ERs) from Liu et al. (2017) with excess DACOM CO mixing ratio from the first WAS sample of the long-axis leg. Normalized excess mixing ratios for the near-source WAS sample are generally within ±50% of the ERs reported by Liu et al. (2017) for the Rim
175 Fire (Fig. S3). The Liu et al. (2017) ERs incorporate multiple near-source intercepts and are more representative of average fire conditions. Actual ERs likely vary among the plume samples; in particular, we might expect older samples to show an increased signature of smouldering relative to flaming due to typical wildfire diurnal progression (Wiggins et al., 2020). Observations, however, do not conclusively indicate an age-dependent trend in ERs. MCE generally declines with age (Fig. S4a), but frequent deviation from the expected wildfire value range of $0.8 - 1.0$ (Akagi et al., 2011) suggests non-emission

180 influence (e.g., background CO_2 variability) that degrades this metric as a combustion phase tracer at later ages. NEMRs for the conserved fire tracers HCN and CH_3CN exhibit some variability (mean/standard deviation = 10 – 15%) but no trend (Fig. S4b), suggesting no systematic change in fire-average ERs (Roberts et al., 2020). Conversely, the trend in total observed NO_y may indicate time-varying emissions (Sect. 3.1.4). Given these ambiguities, constant initial concentrations is a reasonable assumption.

185   Dilution is treated in analogy with Gaussian plume dispersion (Alvarado et al., 2015):

$$\left(\frac{\partial X}{\partial t}\right)_{dil} = \frac{-1}{\tau_g + 2t}(X(t) - X_b) \tag{2}$$

Background concentrations (X_b) are the same as those used for dilution normalization. The Gaussian timescale, τ_g, is constant for each puff and calculated using the analytical solution of the integral of Eq. (2) with CO concentrations at start and end-points. The Gaussian timescale varies from 28 to 760 s for individual puffs (Fig. S5). Such variability is not surprising given
190 the horizontal extent of the fire and differences among trajectories for each puff.

    Model chemistry utilizes the Master Chemical Mechanism (MCMv3.3.1) (Jenkin et al., 2015, 1997; Saunders et al., 2003) with modifications. Additional reactions include photolysis of pernitric acid (Atkinson et al., 2004), reaction of methyl peroxy radical with OH (Assaf et al., 2016; Caravan et al., 2018), reaction of hydroxymethyl hydrogen peroxide (HMHP) with OH (Allen et al., 2018), and oxidation of propadiene (C_3H_4). For the latter, we use the OH reaction rate coefficient of Atkinson
195 and Arey (2003) rather than the 1.8-times slower rate coefficient of Daranlot et al. (2012), based on the similar observed decay rates of propadiene and ethene. Subsequent propadiene chemistry follows the mechanisms of Daranlot et al. (2012) and Xu et al. (2019). We also update rate coefficients for reaction of peroxyacetic acid with OH (Berasategui et al., 2020) and peroxyacyl radicals with HO_2 (Jenkin et al., 2019), which are slower/faster than MCM default values by factors of 123/1.33, respectively. Oxidation of some additional biomass burning VOC (furans, syringol, and guaiacol) is incorporated using an MCM extension
200 developed following recent laboratory and field studies (Coggon et al., 2019; Decker et al., 2019, 2021; Robinson et al., 2021).

    There are multiple potential error sources in the puff model, and many are not easily quantified. We assume constant initial concentrations, but the smoke is a heterogeneous mixture of multiple ages and burning phases. Parameterizations for photolysis and dilution make assumptions about the history of each puff based on the observed evolution along the flight path. Heterogeneous chemistry is explicitly included. Despite all these issues, results will illustrate that the puff model is a reasonable
205 approximation and a useful testbed for probing plume chemistry. Measurement accuracy (Table S1) is typically the dominant uncertainty in observations at high signal/noise ratios, thus we use this to define the uncertainty for model-measurement comparisons.

2.4 Model Scenarios

Model scenarios systematically characterize the effects of varying emissions and chemistry (Table 1). In the base simulation
210 (M0), initial species are limited to observations. This includes three species that are not in the MCM: furan, HMHP, and propadiene. Additional simulations incorporate unmeasured reactive VOC and various HONO sources as detailed below.

Table 1. Summary of model simulations.

Simulation	Description
M0	Base simulation using only measured VOC
M1	M0 + Unmeasured VOC
M2a,b,c	M1 + primary HONO (5, 15, 25 ppbv)
M3a,b,c	M1 + secondary HONO via pNO_3^- photolysis ($J(pNO_3^-)$) scaling factors of 0.5, 1, 2)
M4a,b	M1 + secondary HONO via NO_2 + aerosol ($\gamma(NO_2)$ scaling factors of 1, 1000)

2.4.1 Addition of Unmeasured VOC

215   Simulation M1 incorporates unmeasured VOC using the fire laboratory emissions data of Koss et al. (2018), which includes over 500 compounds and 20 Western US fuel types. We restrict this dataset to 152 compounds with specific molecular assignments and estimated OH reaction rate coefficients (Table S5 of Koss et al. (2018)). Incorporating this data requires 1) estimating initial VOC concentrations, and 2) allocating these VOC to model species. For the first step, we create a composite ER profile for the Rim Fire by comparing the ERs of 11 species reported by both Liu et al. (2017) and Koss et al. (2018):

220   acetylene, ethene, propene, methanol, formaldehyde, acetaldehyde, furan, benzene, toluene, HCN, and CH_3CN. Specifically, we optimize fractional fuel contributions by minimizing the sum square relative error of log-transformed ERs between Liu et al. (2017) and the composite profile. This procedure suggests significant contributions from Jeffrey Pine (34%), Ceanothus (21%), and Manzanita (15%), with lesser contributions from other fuels. Estimated fuel composition is sensitive to which VOC are included in the optimization, as ER profiles are highly correlated among different fuels. For the same reason, model results

225   are not especially sensitive to the choice of fuel composition. Combining composite ERs with observed CO in the first plume sample gives initial mixing ratios. We assume zero background for all unmeasured VOC. ERs for acrolein and biacetyl are reduced by a factors of 2.3 and 10, respectively, due to known calibration issues (SI Text S1).

Unmeasured VOC are assigned to model species in two steps. 51 of these gases appear in the MCM or the extended NOAA biomass burning mechanism. The remaining 101 compounds lack direct MCM analogues. These VOC are allocated

230   to MCM proxies based on OH reaction rate coefficients (k_{OH}) and molecular formulae. For each VOC, we first identify MCM species that are within some threshold (nominally 20%) of the VOC's estimated k_{OH}. We then attempt to filter the MCM species list to include only those containing a similar number of carbon and oxygen atoms (within ±1 the number of each atom). Specific functional groups are not considered. If the molecular formulae criterion is too restrictive (i.e., no species are identified), we only use the k_{OH} criterion. This procedure, though imperfect, optimizes initial OH reactivity and total VOC

235   mass with the available information. Table S2 lists the MCM assignments and ERs for all unmeasured VOC.

2.4.2 Addition of HONO

Several sets of sensitivity simulations explore the impacts of HONO from both primary (emissions) and secondary sources. All of these simulations include the same initial unmeasured VOC as simulation M1. Simulations M2a, b, and c incorporate primary HONO at initial mixing ratios of 5, 15, and 25 ppbv, respectively. The upper end of this range is based on recent work

240 reporting an average $\Delta HONO/\Delta NO_x$ emission ratio of 0.7 ± 0.3 ppbv ppbv^{-1} and an average $\Delta HONO/\Delta CO$ emission ratio of 5.3 ± 5.2 pptv ppbv^{-1} for Western U.S. wildfires (Peng et al., 2020).

Simulations M3a, b, and c incorporate photolysis of particulate nitrate (pNO_3^-):

$$pNO_3^- + h\nu \rightarrow 0.67 HONO + 0.33 NO_2 \tag{R1}$$

The photolysis frequency for reaction R1 is rescaled from that of gas-phase HNO_3 by a factor of 286 following Ye et al. (2017,

245 2018). The mechanism for this reaction is not well understood (Baergen and Donaldson, 2013), and the efficacy of pNO_3^- photolysis likely depends on aerosol composition (Ma et al., 2021). Other studies have estimated photolysis frequencies an order of magnitude or more lower in non-biomass burning environments (Romer et al., 2018; Shi et al., 2021). Particulate nitrate concentrations are constrained by aerosol mass spectrometer (AMS) observations (Fig. S6a). Comparison with other aerosol composition observations suggests minor pNO_3^- contained in coarse mode aerosol excluded by the AMS (Fig. S7). It

250 is not possible to partition AMS pNO_3^- between organic and inorganic forms for SEAC^{4}RS (Ulbrich et al., 2009; Day et al., 2021); however, the nature of particulate nitrate participating in reaction (R1) is also unclear. The model treats pNO_3^- as non-reactive (no chemical production or loss), but it dilutes with a puff-dependent background concentration, chosen such that concentrations match observations at the start and end of each puff. This is a workaround to ensure the model carries reasonable pNO_3^- concentrations throughout the simulation in the absence of explicit model aerosol chemistry. Simulations M3a, b, and

255 c scale the nominal rate of reaction (R1) by factors of 0.5, 1, and 2, respectively.

Simulations M4a and b incorporate reaction of NO_2 on aerosol surfaces:

$$NO_2 \xrightarrow{k_a} HONO \tag{R2}$$

$$k_a = 0.25 v_{NO2} S_a \gamma \tag{3}$$

Here, k_a is the first-order rate coefficient, v_{NO2} is the mean molecular speed of NO_2, S_a is particle surface area density, and γ is

260 the reactive uptake coefficient. We assume that gas diffusion is not a limiting factor for small values of γ (10^{-3} to 10^{-6}). For S_a, we use Laser Aerosol Spectrometer observations (Yu et al., 2016b) scaled up by a factor of 1.7 to account for calibration bias (Fig. S7) and linearly interpolated over plume age. Values of S_a range from 800 to 6600 μm^2 cm^{-3} (Fig. S6b). Parameterization of γ follows a laboratory-derived relationship with solar radiation (Stemmler et al., 2006; Zhang et al., 2019):

$$\gamma = \begin{cases} \alpha J_{NO2}, & Rad \leq 400\ W\ m^{-2} \\ \alpha J_{NO2}(Rad/400)^2, & Rad > 400\ W\ m^{-2} \\ 10^{-6}, & minimum \end{cases} \tag{4}$$

265 Here, J_{NO2} is the NO_2 photolysis frequency, $\alpha = 2.5 \times 10^{-4}$ is a scaling factor, and *Rad* is total solar irradiance. The latter is estimated using trajectory-dependent SZA and the linear relationship between SZA and observed solar irradiance (Fig. S8).

The minimum value of γ follows Aumont et al. (2003). Figures S6c-d show calculated γ and k_a at the end point of each puff, with values in the range of $4 - 11 \times 10^{-6}$ and $0.3 - 4.9 \times 10^{-6}$ s^{-1}, respectively. Simulation M4a uses this default parameterization, while in simulation M4b k_a is multiplied by a factor of 1000. This range spans observed uptake on humic acid (γ = $2 - 8 \times 10^{-5}$ (Stemmler et al., 2006)) and soot (γ = $3.7 - 11 \times 10^{-3}$ (Ammann et al., 1998)) surfaces.

270

We do not consider ground surface HONO sources (Chai et al., 2021), as plume sampling is predominantly in the free troposphere and uppermost mixed layer.

2.4.3 Parameter Optimization

In a final set of simulations, we simultaneously tune initial unmeasured VOC, initial HONO, and pNO_3^- photolysis. For these

275 runs, default values for initial unmeasured VOC concentrations (M1), initial HONO (M2c), and particulate nitrate photolysis rate (M3b) are each independently scaled by factors of 0, 0.25, 0.5, 0.75, and 1. Iterating over all combinations yield 125 simulations. Results from these simulations are analyzed in terms of normalized mean bias (NMB) (Gustafson and Yu, 2012) relative to observed NEMR age profiles.

3. Results

280 ### 3.1 Observations and Base Simulation

We first examine the observed evolution of trace gases in the Rim Fire. Comparison to base simulation output (M0) benchmarks the representation of this chemistry with MCMv3.3.1 and available constraints.

3.1.1 VOC

The downwind evolution of primary VOC illustrates the differing effects of emissions, dilution, and oxidation. We group VOC

285 into four categories: long-lived alkanes, aromatics/intermediate-lived alkenes, short-lived alkenes, and biogenic terpenes. Groups reflect photochemical lifetimes and similarities in model NMB. Figures 2a–d show an example from each category, Fig. S9 shows the time series of all observed VOC, and Fig. S10 shows the normalized mean bias for each VOC calculated over the full simulation.

Long-lived alkanes such as ethane, propane, and butanes do not decay monotonically with plume age (Figs. 2a and

290 S9a–d). NEMRs for these gases peak downwind of the Rim Fire; for example, the highest propane NEMR occurs at an age of 4 h and is 50% higher than the initial value. All model simulations exhibit negative NMB of –26% or less for these gases (Fig. S10). With lifetimes of days or more against OH oxidation, these gases are relatively sensitive to variability in background levels and regional emissions (e.g., anthropogenic or oil/natural gas activities). For example, at an age of 4 h the ethane enhancement is 4 times its background value, whereas the ethene enhancement is a factor of 70. Variability in fire emissions

295 is a less likely explanation for model-measurement mismatch. Reconciliation with the observed increase in NEMRs at an age

of 2 h would require a VOC-to-CO emission ratio increases of 50 – 100%, and we would expect similar changes in other VOC emission ratios (Liu et al., 2017; Permar et al., 2021) that are not observed. These VOC are minor contributors to plume photochemistry; however, this comparison underscores the challenge of accounting for background variability in Lagrangian or pseudo-Lagrangian simulations.

300   The second group, including most aromatics (benzene, toluene, ethyl benzene and xylenes) and several alkenes (ethene and propadiene), exhibits stronger NEMR decays with age (Figs. 2b and S9e–k). Photochemical lifetimes for these gases range from 11 – 48 hours (except for benzene, with a lifetime of 4 – 10 days), thus we expect both emissions and chemistry to influence NEMR variability. Similar to alkanes, longer-lived aromatics display enhancements at 2 – 6 hours of age. Xylenes, ethene and propadiene exhibit a more monotonic decay. The base model NMB is below 8% for the latter three

305   compounds.

        Oxidation controls the trend of short-lived alkenes, including propene, butenes, butadiene, pent-1-ene, and furan (Figs. 2c and S9l–s). These gases have near-zero background mixing ratios and react primarily with OH. Loss via O_3 reaction is < 15% of the total loss rate, and nitrate radical reaction is negligible within these air masses. NEMRs decay rapidly, and the most reactive gases fall below measurement detection limits at later ages. The base model simulation exaggerates this decay,

310   resulting in negative NMB as large as -233% for furan.

        Terpenes (isoprene and α/β-pinene) are also highly reactive, and emissions of these compounds are lost rapidly (Figs. 2d and S9t,u). Around an age of 2 h, however, NEMRs increase beyond those in the near-source sample. A similar pattern appears in the isoprene oxidation products methyl vinyl ketone (MVK) and methacrolein (MACR) (Fig. S12d). Furthermore, this particular sample is uncharacteristically dilute relative to the Lagrangian age (Fig. S2). This evidence suggests that local

315   biogenic emissions mixed with the Rim Fire smoke samples at Lagrangian ages of 2 – 4 hours.
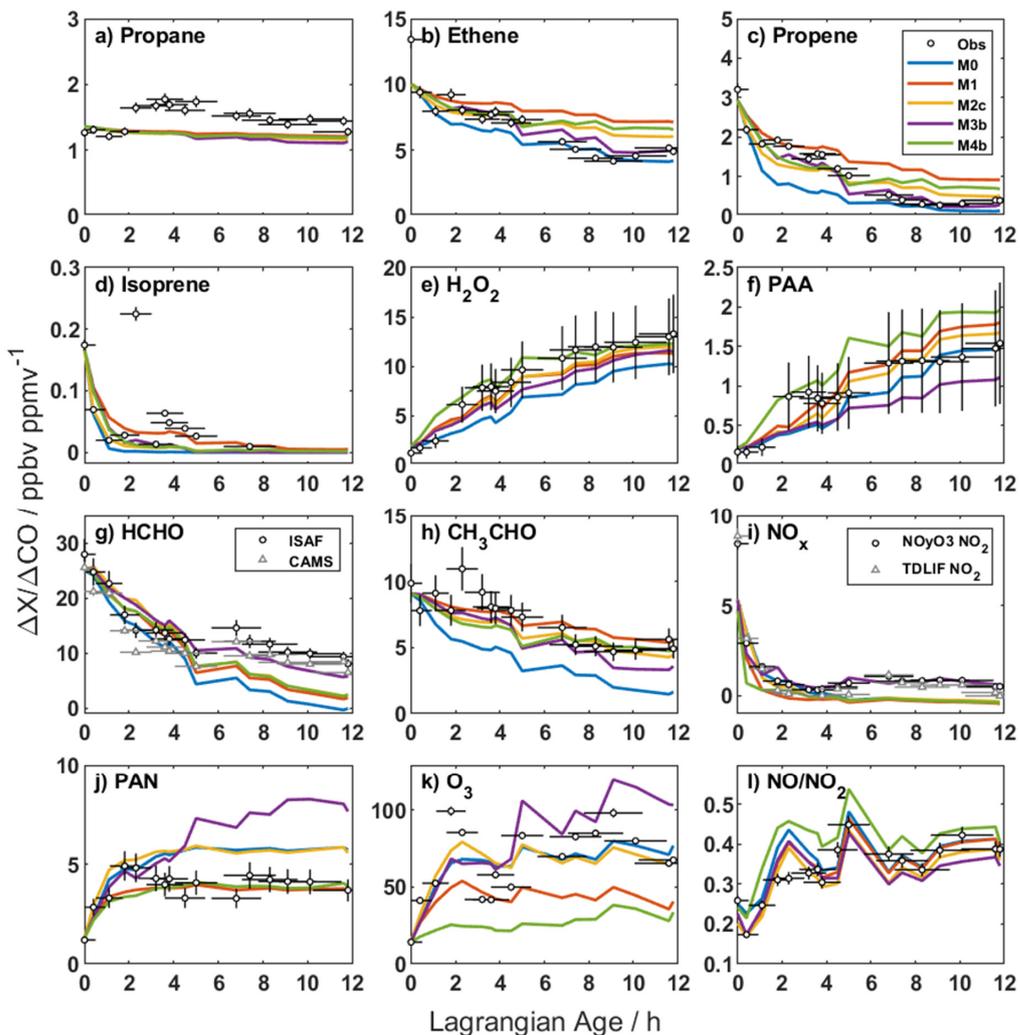
Figure 2. Age evolution of NEMRs for reactive gases (a-k) and the NO/NO₂ ratio (l). Black circles are observations with their corresponding uncertainty due to measurement accuracy and age. Colored lines are model output from the base simulation (M0, blue), addition of unmeasured VOC (M1, red), and addition of unmeasured VOC plus initial HONO (M2c, yellow), pNO₃⁻ photolysis (M3b, purple), or NO₂ heterogeneous uptake (M4b, green). In (g) and (i), circles and triangles represent two independent measurements of HCHO and NO₂, respectively (Table S1). NO and NO₂ observations in (l) are from the NOyO3 instrument.

3.1.2 HO$_x$ and Peroxides

The SEAC^{4}RS DC-8 payload did not include observations of HO$_x$ (= OH + HO$_2$). The loss and production of other compounds, however, indirectly constrains HO$_x$ abundance. The decay rate of short-lived alkenes provides a benchmark for OH, while peroxide production is an indicator for HO$_2$ and, to some extent, RO$_2$.

320   As discussed above, short-lived alkene NEMRs decay faster than observed NEMRs in the base simulation, especially in the first few hours. The discrepancy between modelled and observed short-lived alkenes suggests over-prediction of OH in the young plume. Base model OH starts at 4.9×10^6 cm^{-3} and declines to ~1.2×10^6 cm^{-3} after ~4 hours (Fig. S11a).

    Self-reaction of HO$_2$ produces hydrogen peroxide (H$_2$O$_2$), and reaction of HO$_2$ with peroxyacetyl radical (PA) produces peroxyacetic acid (PAA). NEMRs for both peroxides start low and increase with plume age (Fig. 2e,f). Initial mixing

325 ratios are near background levels, at odds with a previous study suggesting significant primary emissions (Lee et al., 1997). The base simulation exhibits an upward trend but with a slower growth rate, especially over the first 4 hours. Model H$_2$O$_2$ NEMRs skirt the lower edge of measurement accuracy, while PAA agreement generally improves with age. This comparison suggests under-prediction of HO$_2$ and possibly RO$_2$ at early ages. Base model HO$_2$ peaks at ~85 pptv and declines to values as low at 23 pptv (Fig. S11b).

330 3.1.3 Oxygenated VOC

Formaldehyde (HCHO), as an oxidation product of numerous VOC, serves as a top-down constraint on in-plume VOC processing. The observed HCHO NEMR decreases by a factor of three in the first 5 hours before levelling out at later ages (Fig. 2g). This behavior is consistent with loss of primary emissions alongside secondary production (Liao et al., 2021). The HCHO lifetime due to photolysis and OH oxidation is ~3.5 h at the time of sampling, but accumulation of multi-generation

335 oxidation products may sustain downwind HCHO production (Alvarado et al., 2020). The sharp rise in the HCHO NEMR between 5 and 7 hours coincides with descent to a lower sampling altitude (Fig. S1). The base simulation follows observations early on but overestimates the decay at intermediate and later ages.

    The acetaldehyde (CH$_3$CHO) NEMR decay exhibits a more constant slope (Fig. 2h). The small post-emission peak in the acetaldehyde NEMR at an age of 2 h coincides with the aforementioned sharper peaks in biogenic markers and

340 enhancements in long-lived alkanes, which may indicate influence from non-fire surface emissions. Base model NEMRs initially decay more rapidly than observed, but the slope matches observations after the first few hours. This discrepancy is consistent with over-prediction of OH in the young plume, as OH oxidation accounts for 80% of acetaldehyde loss. Conversely, OH only accounts for 15 – 50% of HCHO loss (photolysis is the remainder). Thus, as will be evident in sensitivity simulations discussed later, HCHO and CH3CHO exhibit opposite responses to varying OH.

345   Text S2 and Figure S12 present several other observed oxygenated VOC (oVOC), including methanol, acetone + propanal, hydroxyacetone, and MVK + MACR.

3.1.4 Reactive Nitrogen

Major wildfire reactive nitrogen emissions include NO_x, HONO, and NH_3 (Lindaas et al., 2020; Roberts et al., 2020). Observations of the latter two are not available for SEAC[4]RS, so here we focus on NO_x and observed reservoir species (collectively, NO_y).

The base simulation reasonably reproduces the initial loss of NO_x but does not capture later behavior (Fig. 2i). In the first few hours, the NO_x NEMR decays with an e-folding timescale of 20 – 40 minutes. After reaching a minimum at ~3.6 h, the NO_x NEMR rises to a sustained enhancement at ~10% of the initial value. An additional NO_x source of 200 pptv h[-1] is required to close the NO_x budget in the period between 6 and 12 h. This discrepancy is explored further in Sect. 3.3.

Peroxyacetyl nitrate (PAN) typically comprises the majority of total peroxy nitrates (Wooldridge et al., 2010) and is produced via the reversible reaction of NO_2 with PA. The PAN NEMR rises rapidly in the first two hours before stabilizing (Fig. 2j), comparable to previous observations (Alvarado et al., 2010, 2015). The base simulation captures the early rise in PAN but overshoots the asymptote by ~20%. SI Text S3 and Figures S13-S14 compare model output to measurements of other speciated peroxy nitrates, total peroxy nitrates, and alkyl nitrates, which show varying levels of model-measurement agreement.

Reaction of OH with NO_2 primarily forms nitric acid (HNO_3). The observed HNO_3 NEMR is negative and trends downward with age, indicating that in-plume HNO_3 is below background levels (Fig. S14c). Excess ammonia/ammonium (Perring et al., 2017) likely drives rapid formation of particulate ammonium nitrate (Lindaas et al., 2021). The puff model lacks aerosol chemistry and thus predicts net growth of the HNO_3 NEMR. The difference between the base model and observed HNO_3 NEMR implies an effective HNO_3 lifetime of less than 1 hour.

Figure 3 shows the evolution of the sum of observed NO_y. We refer to this quantity as $\Sigma NO_{y,obs}$ to acknowledge missing observations of some NO_y species such as HONO, HO_2NO_2, and nitroaromatics. The presence of significant PNs within the first sample indicates some chemical aging, as expected for a mixture of smoke ages. After the first hour, PNs comprise more than half of $\Sigma NO_{y,obs}$, pNO_3^- comprises another 20 – 30%, and NO_x and alkyl nitrates contribute 10 – 15% each. The $\Sigma NO_{y,obs}$ NEMR decreases from 18 to 6.3 ppbv ppmv[-1] over 12 hours. In the absence of emission changes and deposition, we expect conservation of the total NO_y NEMR (Juncosa Calahorrano et al., 2020). It seems unlikely that unmeasured NO_y can explain a 2.6-fold decrease over this period (Roberts et al., 2020). Decreasing $\Sigma NO_{y,obs}$ may indicate that NO_x emissions are changing over time or that we are sampling different parts of the Rim Fire with differing NO_x emission ratios. As discussed in Sect. 2.3, evidence regarding emission ratio trends over the sample period is inconclusive. Furthermore, a model simulation assuming declining NO_x emissions with age would further degrade model prediction of observed NO_x at later ages. For comparison, modeled $\Sigma NO_{y,obs}$ (which excludes pNO_3^-) is ~7 ppbv ppmv[-1] throughout simulation M0.
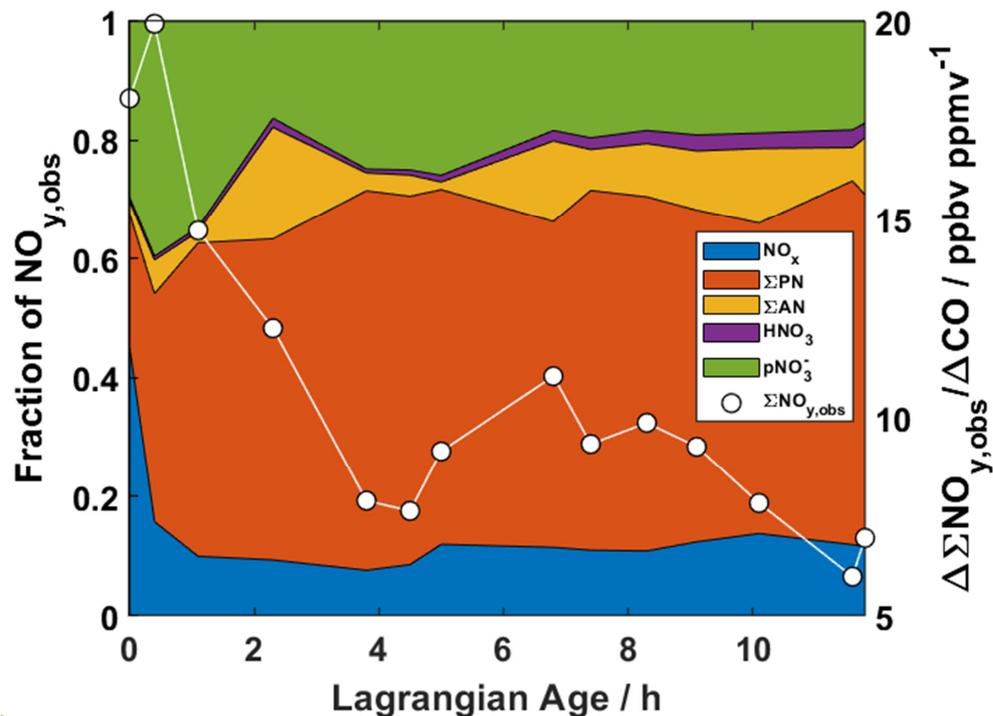
Figure 3. Age evolution of observed NO_y speciation (solid colors, left axis) and the $\Sigma NO_{y,obs}$ NEMR (white circles/line, right axis). $\Sigma NO_{y,obs}$ is the bottom-up sum of observed NO_y. ΣPN represents TDLIF observations.

3.1.5 Ozone

The observed O_3 NEMR grows rapidly within the first few hours before slowing down (Fig. 2k). The peak value at 2 h coincides
380   with the aforementioned peak in biogenic VOC. The base simulation reproduces the general trend of the observed O_3 NEMR
time profile but misses the maximum and under-predicts after 5 h. Significant point-to-point variability in the observed O_3
NEMR mostly reflects variability in the CO excess mixing ratio rather than O_3 itself, as O_3 is relatively close to its background
value. Absolute O_3 reaches a peak of 130 ppbv within the first hour before diluting rapidly to 65 – 75 ppbv, remaining above
the background estimate of 50 ppbv (Fig. S15). Mean absolute bias for base simulation O_3 is -3.2 ppbv averaged over all
385   observations and +0.5 ppbv for ages greater than 2 h.

The ratio of NO to NO_2 relates closely to radical turnover and O_3 production. In the absence of strong NO_x sources
or sinks, photolysis of NO_2 and oxidation of NO establishes a photostationary state that controls this ratio:

$$\frac{[NO]}{[NO_2]} = \frac{J_{NO2}}{k_{NO+O3}[O_3] + k_{NO+HO2}[HO_2] + \sum k_{NO+RO2}[RO_2])} \qquad (5)$$

Here, J_{NO2} is the NO_2 photolysis frequency and k_{X+Y} are reaction rate coefficients. The observed NO/NO_2 ratio doubles over

390   the course 12 hours (Fig. 2l), consistent with the decline of peroxy radicals and ozone mixing ratios. $J(NO_2)$ does not exhibit
a clear trend over this period (Fig. A1). The base simulation over-predicts this ratio in the first few hours and agrees within
uncertainties afterward.

3.2 Accounting for Unmeasured VOC

Differences between observations and the base simulation are consistent with missing reactive VOC in the model. The decay

395   of reactive alkenes is faster than observed, suggesting that model OH is too high. Peroxide and oVOC production is too slow,
indicating missing sources of peroxy radicals and organic carbon. Simulation M1 approximates the effects of unmeasured
VOC, incorporated following the procedures outlined in Sect. 2.4.1.

Total OH reactivity – the inverse of the OH lifetime – increases significantly upon addition of unmeasured VOC (Fig.
4a). Initial OH reactivity grows from 77 to 182 s^{-1}. The top five components of OH reactivity in the observations and simulation

400   M0 are HCHO, CO, CH_3CHO, furan, and propene (Fig. 4c). Species included in simulation M0 comprise ~45% of the OH
reactivity in simulation M1. The top 5 additional contributors in simulation M1 are aromatics, consistent with Coggon et al.
(2019). Enhancements persist as the plume ages, with OH reactivities of 7 s^{-1} (M1) versus 3 s^{-1} (M0) at an age of 12 h. After
12 h, 32% of M1-simulated OH reactivity is comprised of nearly 2200 species, mostly oxygenated VOC.

Normalizing for dilution reveals a more modest decline in OH reactivity due to photochemistry alone (Fig. 4b).

405   Normalized excess OH reactivity declines by 61% and 45% for M0 and M1, respectively. The relatively slower decline in M1
reflects less OH in this simulation. Modelled declines in OH reactivity over 12 h of aging imply a pseudo-first order lifetime
of 12.7 h and 21.4 h for OH reactivity in simulations M0 and M1, respectively. OH reactivity estimates from the model may
be an upper limit, as some reactive carbon will partition to the aerosol phase (Palm et al., 2020).

Additional VOC reactivity markedly alters downwind chemistry. OH decreases to 5×10^5 cm^{-3} for most of the

410   simulation (Fig. S11a), reducing the decay of reactive alkenes to a shallower slope than observed (Fig. 2b–d). Maximum HO_2
increases by 35% (Fig. S11b), and H_2O_2 agrees better with observations (Fig. 2e). PAA increases due to enhanced production
of HO_2 and PA (Fig. 2f). Peroxyacetyl radical is also a PAN precursor, but PAN actually decreases in simulation M1 due to
lower NO_2 (Fig. 2j) and competing formation of larger peroxy nitrates (Fig. S13, S14). Rapid sequestration of NO_x also
suppresses ozone formation in the young plume (Fig. 2k). HCHO and CH_3CHO increase (Fig. 2g–h), but the model still under-

415   predicts HCHO at later ages.
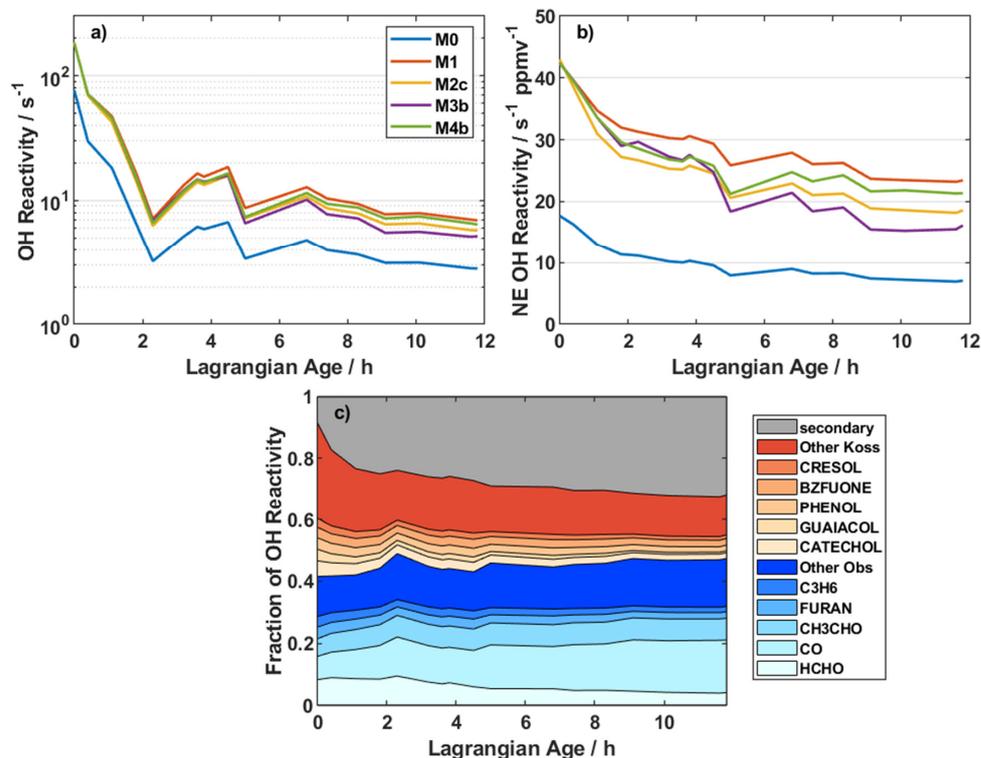
Figure 4. (a) Age evolution of total model OH reactivity, (b) normalized excess OH reactivity, and (c) fractional contributions of individual reactants to total OH reactivity in simulation M1. In (b), normalization is analogous to NEMR calculation (Eq. 1), and the OH reactivity background is 1.1 s^{-1} based on summation over observed OH reactants in the background sample. In (c), blue shades denote measured compounds, red shades are species added from the Koss et al. (2018) inventory, and grey includes all other MCM species reacting with OH.

3.3. Accounting for Primary and Secondary HONO

The contrast of observations and simulation M1 in Fig. 2 implies insufficient OH and NO$_x$. The decay of short-lived alkenes is now slower than observed owing to the large increase in OH reactivity, while the decay of NO$_x$ is faster than observed due to rapid peroxy nitrate formation. Both low OH and low NO$_x$ contribute to under-prediction of O$_3$.

420   Potential explanations for the model-measurement discrepancy in NO$_x$ include NO$_2$ measurement artefacts, emissions variability, unaccounted-for recycling via NO$_x$ reservoirs, and missing NO$_x$ sources. NO$_2$ measurement artefacts are unlikely to play a significant role, given the excellent correlation between two independent NO$_2$ measurements and the magnitude of model-measurement disagreement (Text S3). Doubling initial NO$_x$ has a minor effect on the simulated NO$_x$ NEMR after ~5 h (Fig. S16), and total observed NO$_y$ decreases with Lagrangian age (Fig. 3); thus, NO$_x$ emissions variability also cannot explain

425 this difference. Recycling via decomposition or oxidation of NO_x reservoirs, such as organic nitrates, should be adequately
captured by simulation M1 as the NEMRs of total peroxy nitrates and alkyl nitrates are simulated well (Fig. S13 and S14). We
lack observations of HO_2NO_2 or $CH_3O_2NO_2$, but lifetimes for these gases are a few minutes for our conditions and modelled
mixing ratios are less than 10 pptv after 5h. Nitroaromatic photolysis may generate HONO (Sangwan and Zhu, 2016), but
these compounds do not build up to sufficient levels to act as a major NO_x source in the model. Therefore, a missing NO_x
430 source is the most likely explanation.

Previous work has demonstrated the important role of HONO in smoke plume chemistry (Alvarado et al., 2015;
Alvarado and Prinn, 2009; Peng et al., 2020; Theys et al., 2020). Direct HONO emissions amplify radical production in the
nascent plume, while secondary HONO formation may sustain chemistry as the plume ages. As discussed in Sect. 2.4.1 and
summarized in Table 1, we implemented both primary emissions (simulations M2a,b,c) and secondary production via pNO_3^-
435 photolysis (M3a,b,c) or heterogeneous NO_2 reaction (M4a,b). Figure S17 shows the HONO NEMR and absolute mixing ratio
for several representative simulations. The HONO photolysis lifetime, based on observed photolysis frequencies, is 10 – 20
minutes. HONO mixing ratios in simulations with secondary production (M3b and M4b) are 10's of pptv after a few hours.
Most figures in the main text and supplement display results from simulations with high primary HONO (M2c), moderate
pNO_3^- photolysis (M3b) and fast NO_2 heterogeneous uptake (M4b), while Figures S18 – S20 show full results for each
440 sensitivity series.

Initial HONO stimulates chemistry in the first several hours. Simulation M2c starts with 25 ppbv of HONO,
comparable to levels observed in other Western U.S. wild fires (Peng et al., 2020). Photolysis of HONO increases OH and NO
production, leading to faster VOC decay and product formation (Fig. 2 and S11). Intensification is limited to the first few
hours, and the decay of short-lived alkenes, like propene and butenes, is too slow at later ages (Fig. 2c). NO_x agreement also
445 improves at early times, but under-prediction persists after 3 h of aging (Fig. 2i). PAN and O_3 profiles are close to those in the
base simulation (Fig. 2j-k).

Photolysis of pNO_3^- leads to more sustained impacts. Simulation M3b uses the literature-derived rate for reaction R1
(Ye et al., 2017). For this case, median OH increases by a factor of 3.5 relative to simulation M1 (Fig. S11), improving model
agreement with short-lived VOC (Fig. 2b-c). HO_2 is mostly unchanged, reflecting a counterbalance of faster production via
450 VOC oxidation and faster loss via reaction with NO. Unique to the mechanisms tested in this study, pNO_3^- photolysis
reproduces the enhancements in HCHO and NO_x NEMRs observed at later ages (Fig. 2g, 2i). On the other hand, PAN and
ozone are now over-predicted (Fig. 2j, 2l), as are ΣPN and some speciated PNs (Fig. S13, S14). Halving the pNO_3^- photolysis
rate improves agreement with PAN and O_3 at the expense of NO_x and HCHO (Fig. S19, compare simulations M3a and M3b).
Over-prediction of PAN and its analogues in these simulations may reflect errors in the VOC distribution and/or chemical
455 kinetics (Sect. 4.2). These simplified simulations also do not capture age-dependent variability in aerosol composition (e.g.,
organic versus inorganic pNO_3^-), which could influence the effective pNO_3^- photolysis rate and product yields.

In contrast to the above, HONO production via heterogeneous reaction of NO_2 generally degrades agreement with
observations (Fig. S19). Results from simulation M4a are nearly identical to those from M1, while in simulation M4b (γ

multiplied by 1000) ozone and NO_x under-prediction worsens. With rapid HONO photolysis, this process effectively converts
460   NO_2 to NO while producing OH. This increases the loss of O_3 to reaction with NO (reflected in the NO/NO_2 ratio), reducing
net O_3 production. NO_2 conversion to HONO is nearly NO_x-neutral, whereas pNO_3^- photolysis is effectively a NO_x source.

3.4 Co-optimization of VOC and HONO

Additional reactive VOC and HONO chemistry act together to improve model-measurement agreement for most species.
HONO sensitivity simulations presented in Sect. 3.3 utilize the same initial VOC as simulation M1. Uncertainties in initial
465   VOC concentrations stem from the age distribution and history of sampled smoke, adaptation of laboratory-derived emission
factors to ambient conditions, potential errors in the emission factors themselves (SI Text S1), and translation of unmeasured
VOC to MCM species. Uncertainties in primary and secondary HONO are also significant, as we lack a HONO measurement
for comparison and putative aerosol mechanisms are not well understood.

       To illustrate the co-dependence of VOC and HONO, we simultaneously scale initial unmeasured VOC, initial HONO,
470   and pNO_3^- photolysis as described in Sect. 2.4.3. We ignore NO_2 heterogeneous uptake here and focus analysis on O_3. For
each of the 125 simulations, we first calculate the NMB of the O_3 NEMR. Consistent with the examples presented above, this
bias trends negative with increasing VOC and positive with increasing HONO (Fig. S21a-e). Multiple scaling combinations
produce a net O_3 NEMR NMB near zero (Fig. 5). In general, increasing initial unmeasured VOC concentrations necessitates
higher HONO to maintain agreement with observed O_3. Initial and secondary HONO similarly influence the overall O_3 NEMR
475   NMB, though this simplified metric masks age-dependent differences (Fig. 5 inset).

       Figure S22 shows similar minimum NMB isopleths for NO_x and PAN NEMRs. Overall behavior is relatively similar.
Compared to O_3, higher HONO is required to close the NO_x budget. PAN bias is minimized at higher VOC, but only with low
initial HONO and relatively slow pNO_3^- photolysis. No combination of scaling factors optimizes agreement among all
observations.
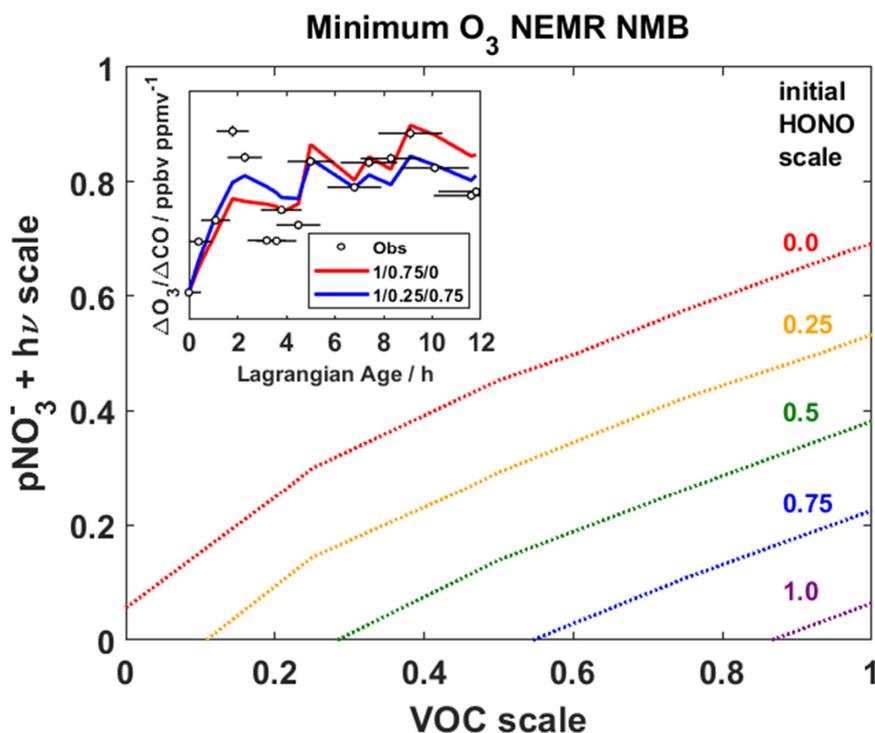
Figure 5. Isopleths for zero values of the O₃ NEMR NMB. Each colored dotted line represents a fixed scaling factor for initial HONO mixing ratios. The x-y coordinates for a point on a given line represent a combination of VOC and pNO₃⁻ photolysis scaling factors that minimize the O₃ NEMR NMB. Isopleths are based on interpolation of results from the optimization simulations (Fig. S21). The inset compares observed O₃ NEMRs with those from two simulations with near-zero NMB (red: VOC scale = 1, pNO₃⁻ + hν scale = 0.75, initial HONO scale = 0; purple: VOC scale = 1, pNO₃⁻ + hν scale = 0.25, initial HONO scale = 0.75).

4 Discussion

4.1 Radical Production and Fate

Inclusion of additional reactive VOC and HONO significantly accelerates radical throughput. Figures 6a-b summarize rates of key RO_x ($OH + HO_2 + RO_2 + RO$) production and loss pathways integrated over the first 2.3 hours of plume aging, where NEMRs change most rapidly. Compared to the base simulation, total RO_x initiation and termination doubles in simulation M1 (VOC addition) and more than triples in M2c (initial HONO). As illustrated in Sect. 3, these changes influence the lifetime of reactive gases and the production of secondary compounds such as ozone, peroxides, organic nitrates, and oVOC. Comparison of O₃ NEMRs in Fig. 2k, however, also demonstrates simulation of an ozone profile that reasonably matches observations

even with missing processes. Constraints on other aspects of the chemical system facilitate holistic evaluation of additional chemistry.

490   Photolysis sources dominate radical initiation (Fig. 6a). Photolysis of O_3 to O^1D and H_2O_2 are each less than 2% of total production in all simulations. In the base simulation, photolysis of HCHO and other oVOC comprises 75% of the radical source. Enhanced reactive VOC in simulation M1 doubles the initiation rate, mainly via further oVOC photolysis and alkene ozonolysis. The largest contributors in the former category are glyoxal (19%) and methyl glyoxal (15%). HONO photolysis in simulations M2 – M4 further accelerates initiation. Simulation M2c (initial HONO) exhibits the most substantial increase of

495   the plotted simulations, with HONO photolysis comprising 33% of initiation. The relative contribution of HONO is smaller here than in other recent studies (Peng et al., 2020; Robinson et al., 2021) for two reasons. First, we average over the first 2 hours of aging, and the lifetime of HONO is tens of minutes. Second, incorporation of an extended VOC pool greatly enhances oVOC photolysis. There is uncertainty in this contribution due to MCM mapping of VOC (Table S2). Nonetheless, studies failing to account for all oVOC might under-predict radical initiation and over-estimate the relative importance of other radical

500   sources.

    Radical termination includes significant contributions from both RO_x-RO_x and RO_x-NO_x reactions (Fig. 6b). Formation of peroxides comprises most of the former group, with equal contributions from $HO_2 + HO_2$ and $RO_2 + HO_2$ in simulation M0. Addition of reactive VOC in M1 doubles the rate of $HO_2 + HO_2$ and triples the rate of $RO_2 + HO_2$. PN formation comprises 65 – 86% of RO_x-NO_x termination, with larger contributions at higher VOC and higher initial HONO. Pernitric acid

505   formation ($HO_2 + NO_2$) is 18% of RO_x-NO_x termination in simulation S2c, reflecting fast formation in the concentrated plume followed by rapid dilution (i.e., dilution outpaces thermal decomposition). Contributions of nitric acid ($OH + NO_2$) and nitroaromatic ($ArNO_2$) formation are 3 – 15% and 0.1 – 6% of RO_x-NO_x termination, respectively. The "OH + X" group includes reaction of OH with HONO and PNs to form NO_2 and other products. These reactions remove RO_x, but they are not strictly radical termination.

510   The balance of RO_x loss via NO_x and RO_x sinks, typically represented as the ratio of NO_x-related loss (L_N) to total radical loss or production (Q), quantifies the sensitivity of ozone production to VOC and NO_x availability (Kleinman et al., 1997; Kleinman, 2005). Here we define L_N as the sum of losses via formation of ANs, PNs, nitroaromatics, nitric acid, and pernitric acid (blue-shaded reactions in Fig. 6b). Traditionally, the assumption that HNO_3 formation is the dominant NO_x sink implies a transition from VOC to NO_x-sensitive O_3 production at $L_N/Q = 0.5$ (Kleinman et al., 1997). Significant organic nitrate

515   formation alters this threshold (Robinson et al., 2021; Schroeder et al., 2017). We adopt a threshold of $L_N/Q = 0.41$ based on a recent study of Western U.S. wildfires (Robinson et al., 2021).

    Ozone production in the young plume is sensitive to both VOC and NO_x (Fig. 6c). All plotted simulations start with a ratio around 0.8 (VOC-sensitive) and transition to NO_x-sensitive within the first hour. This rapid shift is consistent with afternoon aging in other Western U.S. wildfires (Robinson et al., 2021) and reflects sequestration of NO_x within PNs and other

520   organic nitrates. Addition of VOC in simulation M1 accelerates this transition (more RO_x), while HONO slows the transition

in M2c and M3b. Simulation M4b exhibits the fastest transition, where NO_2 conversion to HONO amplifies RO_x while mitigating PAN formation.

The consequences of secondary chemistry assumptions become more apparent at later ages. Most simulations decay to steady L_N/Q values of 0.03 – 0.06 after 5 hours of aging. Simulation M3b is the exception, maintaining L_N/Q around 0.2 due

525   to a sustained NO_x source via pNO_3^- photolysis. The accuracy of this simulation is dubious due to a lack of HONO observations; however, the contrast between M3b and M4b illustrates divergent effects of HONO production mechanisms on radical chemistry. Such differences can affect sensitivity to downwind perturbations, such as when mixing with urban (high NO_x) or biogenic (high VOC) air.
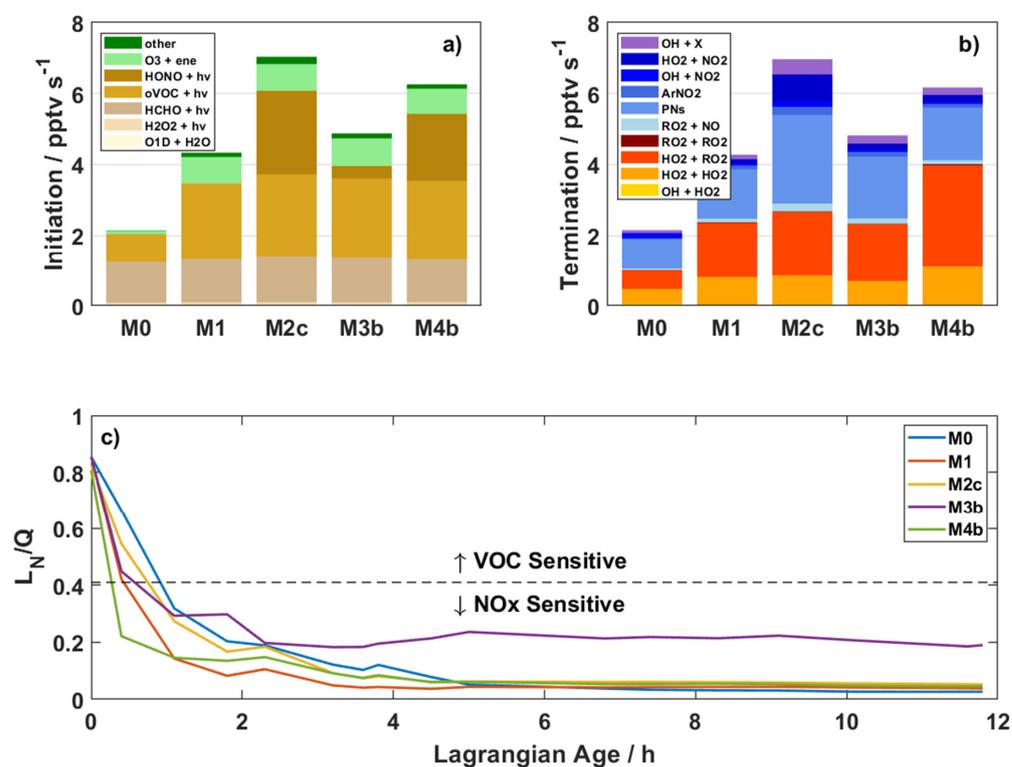
Figure 6. Upper: rates of RO_x initiation (a) and termination (b) integrated over the first five data points (Lagrangian age 0 – 2.3 hours) via trapezoidal integration. In (a), "oVOC + hv" includes all oVOC photolysis reactions other than HCHO and "other" includes NO_3 + VOC and other minor reactions. In (b), yellow-red and blue shades represent RO_x-RO_x and RO_x-NO_x reactions, respectively. "ArNO2" represents formation of nitroaromatics and "PNs" is net formation of peroxy nitrates. "OH + X" (purple) represents reactions of OH with organic compounds (typically PNs), which result in formation of NO_2 and other non-RO_x products. Lower: Fraction of RO_x radicals lost via reactions with NO_x (c). Model simulations are as described in Fig. 2 and Table 1. The dashed line denotes the approximate transition between NO_x-sensitive and VOC-sensitive ozone production for biomass burning chemistry as suggested by Robinson et al. (2021).

4.2 Implications for Modelling Biomass Burning Chemistry

530   Box model deficiencies temper the above results and underscore the challenges of simulating smoke plume chemistry. Simulations including both unmeasured reactive VOC and initial HONO or pNO_3^- photolysis (M2c or M3b) reasonably match observed NEMRs in the first 2 hours of aging (Fig. 2); however, none of the scenarios explored here simultaneously reconcile O_3, NO_x, and PAN throughout the whole sample period. Errors due to assumptions about emissions and air mass history may become more significant further downwind; for example, the model does not capture the large decline in total observed NO_y

535   (Fig. 3). Better observations of emission and background variability would reduce uncertainty, although this can be logistically challenging for large smoke plumes like the Rim Fire.

     Errors in kinetics or VOC speciation may also contribute to model uncertainties. For example, our mechanism includes updated reaction rate coefficients for PA + HO_2 (faster by a factor of 1.33) and PAA + OH (slower by a factor of 123) based on recent laboratory results (Berasategui et al., 2020; Jenkin et al., 2019). Using MCM default values instead reduces model

540   PAA NEMRs by half (results not shown). Analogous changes to other aspects of the mechanism, due to yet-unrecognized systematic errors, could influence other species. Over-prediction of PAN in simulations M2c and M3b may reflect errors in the thermal equilibrium, the NO/NO_2 ratio (under-predicted at later ages in simulation M3b), and/or VOC speciation. Regarding the last issue, acetaldehyde oxidation comprises half of PA production in our simulations, while the other half stems from mostly unmeasured precursors like methyl glyoxal (24% of production) (Fig. S23). Observations of major PAN

545   precursors are necessary to close the PAN budget. Observations of PNs with specific precursors also afford complementary information; for example, over-prediction of APAN in most scenarios (Fig. S13) may imply that initial acrolein is too high. Observations of HONO, HO_2NO_2, and total NO_y would also help to fully constrain radical sources, cycling, and fate.

     For regional and global models, whether and how to account for the full VOC distribution remains an open challenge. Advances in instrumentation have facilitated quantification of myriad reactive gases (Heald and Kroll, 2020). Cumulatively,

550   individually minor species can comprise a significant fraction of OH reactivity and potential organic aerosol mass (Gilman et al., 2015). Condensed mechanisms cannot represent this level of speciation. One option to reduce this complexity, similar to our methodology, is to identify proxy or surrogate species within a given mechanism based on mass, molecular formula, reactivity, volatility, or other metrics. Given the variability of chemistry within smoke plumes, machine learning techniques may also prove useful for condensing VOC into a manageable framework (Kelp et al., 2020). Multifaceted observations can

555   help ensure accurate representation of key chemical processes that influence the spatial and temporal extent of air quality and climate impacts.

       Many atmospheric chemistry models do not incorporate primary emissions or heterogeneous production of HONO in standard simulations, including GEOS-Chem (L. Hu, personal communication, 2021). Primary HONO is a key oxidant source in young fire plumes (Peng et al., 2020). The HONO photolysis lifetime of 10 – 20 minutes can be on the order of, or much

560   shorter than, an advection timescale for a single grid cell (e.g., a 12 km grid cell at a wind speed of 10 m s^{-1} has an advection timescale of 20 minutes). Thus, "instantaneous dilution" may be a major hurdle to simulating this fast chemistry. Plume

heterogeneity (e.g., a darker core) also confounds efforts to simulate chemistry in an average sense (Wang et al., 2021). Putative secondary HONO sources are manifold (Zhang et al., 2019), as are associated uncertainties. A recent lab study of pNO_3^- photolysis on inorganic aerosol suggests a ten-times slower photolysis rate than assumed in simulation M3b (Shi et al., 2021),

565 and a similar reduction was derived from an analysis of NO_y partitioning in polluted marine air (Romer et al., 2018). Further lab work has shown that the rate and product yield of this reaction is sensitive to surface composition (Ma et al., 2021). Robust parameterizations will require continued systematic study of controlling factors, preferably under environmentally relevant and near-ambient conditions.

Wildfire emissions may have a more sustained influence on regional background chemistry than is currently

570 appreciated. Synergistic increases in OH reactivity and oxidants in our sensitivity simulations stimulate production of multi-generation oxygenated VOC and organic NO_x reservoirs like PAN, altering the spatiotemporal scale of ozone and organic aerosol production. The modest decline of normalized excess OH reactivity (Fig. 4b) further implies that active chemistry persists far downwind. For example, the 62% decrease over 11.8 h of aging in simulation M3b implies an effective pseudo-first-order photochemical lifetime of 12.2 h for the total OH sink. This aligns with a recent analysis of satellite observations

575 suggesting an effective lifetime of 20 hours or more for formaldehyde and glyoxal in aging smoke plumes (Alvarado et al., 2020). Space-based remote sensing of atmospheric composition may aid evaluation of model biomass burning emissions and chemistry on these scales.

5 Conclusions

Using a 0-D puff model constrained with SEAC[4]RS in situ observations, we have examined the gas-phase chemical evolution

580 of the 2013 California Rim Fire plume and illustrated the sensitivity of chemistry to unmeasured reactive VOC and HONO. The rich measurement suite permits a holistic evaluation of the various components of the chemical system, including VOC, HO_x, NO_y, and O_3. Initializing with observed gases only, the model reasonably reproduces the evolution of O_3 over 12 hours of aging but fails in other key aspects, including over-prediction of reactive VOC decay rates and under-prediction of NO_x and HCHO. Accounting for additional VOC identified by recent laboratory studies increases OH reactivity more than twofold

585 throughout the simulation, drawing down model OH and generally degrading performance. Subsequent addition of HONO amplifies radical production and cycling. Addition of initial HONO (assumed to be primary emissions) or secondary production via pNO_3^- photolysis improves predictions of ozone, oVOC, and NO_x, while HONO production via NO_2 heterogeneous conversion generally degrades model performance. Further "optimization" simulations demonstrate that multiple combinations of enhanced VOC and primary/secondary HONO can minimize model-measurement bias with respect

590 to O_3 and NO_x, although we cannot reconcile the model with all observations simultaneously. Examination of model reaction rates over the first 2.3 hours of aging demonstrates the potentially dominant contribution of oVOC photolysis to radical initiation, the importance of PN formation as a NO_x sink, and the competitive roles of RO_x-RO_x and RO_x-NO_x reactions in radical termination. Ozone production is sensitive to both VOC and NO_x in the young plume for all sensitivity simulations.

Ozone production transitions from VOC-sensitive to NO_x-sensitive after ~1 hour of aging. The timing of this transition depends

595   on VOC and HONO. Downwind NO_x sensitivity depends on the nature and efficacy of assumed secondary HONO/NO_x sources.

A primary finding of this study is that reactive VOC and oxidant sources are complementary in the wildfire-influenced atmosphere, and consideration of both is necessary for accurate simulation of near- and far-field impacts on atmospheric composition, air quality, and radiative forcing. Future efforts must focus on an efficient solution for incorporating this

600   somewhat novel chemistry in regional and global models, or else quantify the uncertainty associated with neglecting it.

This work also demonstrates the value of a near-comprehensive payload afforded by a heavy-lift aircraft like the NASA DC-8. The breadth of information in the SEAC[4]RS dataset enables a holistic examination of individual aspects of the chemical system within the context of the whole. Ongoing analysis of data from FIREX-AQ, WE-CAN, and similar missions will illuminate the factors driving variability in reactive VOC, HONO, and other key aspects of fire plume chemistry. This

605   same approach is beneficial to investigation of other complex environments (urban, biogenic, etc.) that comprise the lower troposphere.

Appendix A. Photolysis Parameterization

For each puff, photolysis frequency J at solar time t (and a corresponding Lagrangian plume age) is calculated as

$$J(t, age) = sJ_{cs}(t)/r(age) \tag{A1}$$

610   Here, $J_{cs}(t)$ is the clear-sky photolysis frequency and s and $r(age)$ are observation-based scaling factors. Clear-sky photolysis frequencies stem from F0AM's hybrid parameterization, which combines solar spectra from the tropospheric ultraviolet and visible radiative transfer model (TUVv5.2, available at https://www2.acom.ucar.edu/modeling/tropospheric-ultraviolet-and-visible-tuv-radiation-model) with literature-recommended cross sections and quantum yields. This calculation uses actual SZA and measurement altitude and assumes and an overhead ozone column of 290 DU and a surface albedo of 0.01. The age-

615   dependent scaling factor $r(age)$ is determined by fitting the ratio of clear-sky to observed photolysis frequencies as a function of Lagrangian age using a modified exponential:

$$r(age) = r_0 e^{-age/\tau} + r_\infty \left(1 - e^{-age/\tau}\right) \tag{A2}$$

Here, r_0, r_∞, and τ are fitting coefficients that depend on J. Figure A1 illustrates this fit for ozone and NO_2 photolysis frequencies, which are suppressed by as much as a factor of 3.2 and 1.9, respectively, in the fresh plume. Fits capture 83 –

620   92% of the variability in the clear-sky to observed ratio for all J-values, with the exception of two points with ages of 1 – 2 hours. These points are not included in the fit as they appear to be outliers, especially for $J(O^1D)$, and their inclusion would significantly degrade overall fit quality. It is unclear why these points differ from the overall trend, as no other dilution or chemical markers show exceptional behavior at these times. The age correction is the same for all puffs. The other parameter, s, is a scalar multiplicative factor that adjusts model J-values to agree with observations at trajectory endpoints (analogous to

625   the scaling applied for trajectory meteorology) and is different for each puff.
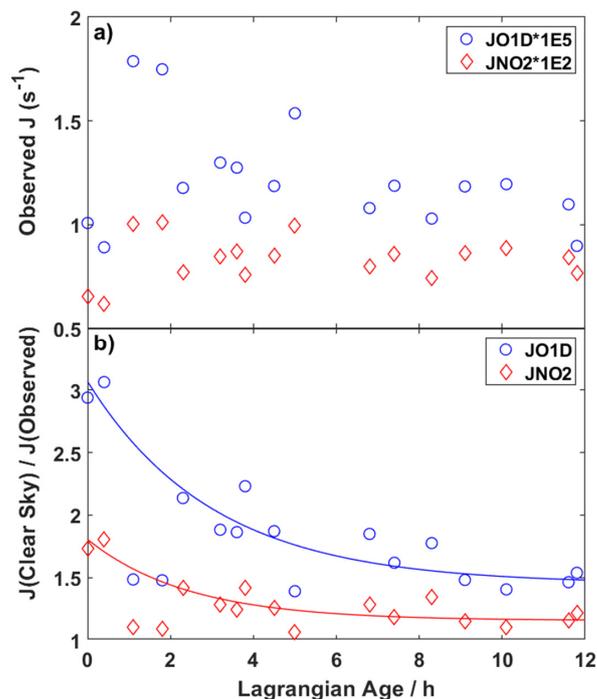
Figure A1. (a) Average observed photolysis frequencies for each WAS sample for O$_3$ → O(^{1}D) + O$_2$ (blue circles) and NO$_2$ → NO + O(^{3}P) (red diamonds). (b) Ratio of clear-sky to observed photolysis frequencies. Clear-sky values are calculated using TUV solar spectra and F0AM parameterizations. Lines represent least-squares fits to Eq. (A2). The two points between ages of 1 – 2 hours are excluded from the fit.

Data and Code Availability

Data used in this study is archived at http://doi.org/10.5067/Aircraft/SEAC4RS/Aerosol-TraceGas-Cloud. The F0AM box model is available at https://github.com/AirChem/F0AM. Model setup code is available from the contact author upon request.

Author Contributions

630   GMW conceptualized the study, conducted the modelling and analysis, and wrote the publication. All authors contributed to data curation and review of the manuscript.

Competing interests

Some authors are members of the editorial board of ACP. An independent editor guided the peer review process, and the authors have no other competing interests to declare.

635 **Acknowledgements**

The SEAC[4]RS mission was supported by the NASA Tropospheric Composition program and grants from the NASA ROSES SEAC[4]RS program (NNH10ZDA001N, NNX12AC03G, NNX12AB82G). We thank the DC-8 pilots, crew, payload operators and mission scientists for their hard work and dedication. We thank Luke Ziemba, Lee Thornhill, and the LARGE team for LAS data. We thank Anthony Bucholtz for BBR data. We are also grateful to NASA ESPO for mission logistics. Analysis and
640 modeling were supported by NOAA Climate Program Office's Atmospheric Chemistry, Carbon Cycle, and Climate program (NA17OAR4310004). The Jimenez group acknowledges support from NASA grants 80NSSC19k0124 and 80NSSC18K0630. PTR-MS measurements during SEAC[4]RS were supported by the Austrian Federal Ministry for Transport, Innovation and Technology (bmvit) through the Austrian Space Applications Programme (ASAP) of the Austrian Research Promotion Agency (FFG). A.W. and T.M. received support from the Visiting Scientist Program at the National Institute of Aerospace (NIA). We
645 thank many colleagues for their assistance, insight and feedback, including Steve Brown, Christine Wiedinmyer, Sarah Strode, Ann Marie Carlton, Matt Coggon, Jim Roberts, Joel Thornton, and Qiaoyun Peng.

References

Adler, G., Wagner, N. L., Lamb, K. D., Manfred, K. M., Schwarz, J. P., Franchin, A., Middlebrook, A. M., Washenfelder, R. A., Womack, C. C., Yokelson, R. J., and Murphy, D. M.: Evidence in biomass burning smoke for a light-absorbing aerosol
650 with properties intermediate between brown and black carbon, 53, 976–989, https://doi.org/10.1080/02786826.2019.1617832, 2019.

Akagi, S. K., Yokelson, R. J., Wiedinmyer, C., Alvarado, M. J., Reid, J. S., Karl, T., Crounse, J. D., and Wennberg, P. O.: Emission factors for open and domestic biomass burning for use in atmospheric models, 11, 4039–4072, https://doi.org/10.5194/acp-11-4039-2011, 2011.

655 Akagi, S. K., Craven, J. S., Taylor, J. W., Mcmeeking, G. R., Yokelson, R. J., Burling, I. R., Urbanski, S. P., Wold, C. E., Seinfeld, J. H., Coe, H., Alvarado, M. J., and Weise, D. R.: Evolution of trace gases and particles emitted by a chaparral fire in California, 12, 1397–1421, https://doi.org/10.5194/acp-12-1397-2012, 2012.

Akagi, S. K., Yokelson, R. J., Burling, I. R., Meinardi, S., Simpson, I., Blake, D. R., McMeeking, G. R., Sullivan, A., Lee, T., Kreidenweis, S., Urbanski, S., Reardon, J., Griffith, D. W. T., Johnson, T. J., Weise, D. R., Chemistry, A., Atmospheric, P.,
660 and Techniques, M.: Measurements of reactive trace gases and variable O-3 formation rates in some South Carolina biomass burning plumes, 13, 1141–1165, https://doi.org/10.5194/acp-13-1141-2013, 2013.

Allen, H. M., Crounse, J. D., Bates, K. H., Teng, A. P., Krawiec-thayer, M. P., Rivera-rios, J. C., Keutsch, F. N., Clair, J. M. S., Hanisco, T. F., Møller, K. H., Kjaergaard, H. G., and Wennberg, P. O.: Kinetics and Product Yields of the OH Initiated Oxidation of Hydroxymethyl Hydroperoxide, 122, 6292–6302, https://doi.org/10.1021/acs.jpca.8b04577, 2018.

665 Alvarado, L. M. A., Richter, A., Vrekoussis, M., Hilboll, A., Kalisz Hedegaard, A. B., Schneising, O., and Burrows, J. P.: Unexpected long-range transport of glyoxal and formaldehyde observed from the Copernicus Sentinel-5 Precursor satellite during the 2018 Canadian wildfires, 20, 2057–2072, https://doi.org/10.5194/acp-20-2057-2020, 2020.

Alvarado, M. J. and Prinn, R. G.: Formation of ozone and growth of aerosols in young smoke plumes from biomass burning: 1. Lagrangian parcel studies, 114, https://doi.org/10.1029/2008jd011144, 2009.

670 Alvarado, M. J., Logan, J. A., Mao, J., Apel, E., Riemer, D., Blake, D., Cohen, R. C., Min, K. E., Perring, A. E., Browne, E. C., Wooldridge, P. J., Diskin, G. S., Sachse, G. W., Fuelberg, H., Sessions, W. R., Harrigan, D. L., Huey, G., Liao, J., Case-Hanks, A., Jimenez, J. L., Cubison, M. J., Vay, S. A., Weinheimer, A. J., Knapp, D. J., Montzka, D. D., Flocke, F. M., Pollack, I. B., Wennberg, P. O., Kurten, A., Crounse, J., Clair, J. M. S., Wisthaler, A., Mikoviny, T., Yantosca, R. M., Carouge, C. C., and Le Sager, P.: Nitrogen oxides and PAN in plumes from boreal fires during ARCTAS-B and their impact on ozone: an 675 integrated analysis of aircraft and satellite observations, 10, 9739–9760, https://doi.org/10.5194/acp-10-9739-2010, 2010.

Alvarado, M. J., Lonsdale, C. R., Yokelson, R. J., Akagi, S. K., Coe, H., Craven, J. S., Fischer, E. V, McMeeking, G. R., Seinfeld, J. H., Soni, T., Taylor, J. W., Weise, D. R., and Wold, C. E.: Investigating the links between ozone and organic aerosol chemistry in a biomass burning plume from a prescribed fire in California chaparral, 15, 6667–6688, https://doi.org/10.5194/acp-15-6667-2015, 2015.

680 Ammann, M., Kalberer, M., Jost, D. T., Tobler, L., Rössler, E., Piguet, D., Gäggeler, H. W., and Baltensperger, U.: Heterogeneous production of nitrous acid on soot in polluted air masses, 395, 157–160, https://doi.org/10.1038/25965, 1998.

Andreae, M. O.: Emission of trace gases and aerosols from biomass burning - An updated assessment, 19, 8523–8546, https://doi.org/10.5194/acp-19-8523-2019, 2019.

Assaf, E., Song, B., Tomas, A., Schoemaecker, C., and Fittschen, C.: Rate Constant of the Reaction between CH3O2 Radicals 685 and OH Radicals Revisited, 120, 8923–8932, https://doi.org/10.1021/acs.jpca.6b07704, 2016.

Atkinson, R. and Arey, J.: Atmospheric degradation of volatile organic compounds, 103, 4605–4638, 2003.

Atkinson, R., Baulch, D. L., Cox, R. A., Crowley, J. N., Hampson, R. F., Hynes, R. G., Jenkin, M. E., Rossi, M. J., and Troe, J.: Evaluated kinetic and photochemical data for atmospheric chemistry: Volume I - gas phase reactions of O-x, HOx, NOx and SOx species, 4, 1461–1738, 2004.

690 Aumont, B., Chervier, F., and Laval, S.: Contribution of HONO sources to the NOx/HOx/O3 chemistry in the polluted boundary layer, Atmospheric Environment, 37, 487–498, https://doi.org/10.1016/S1352-2310(02)00920-2, 2003.

Baergen, A. M. and Donaldson, D. J.: Photochemical Renoxification of Nitric Acid on Real Urban Grime, Environ. Sci. Technol., 47, 815–820, https://doi.org/10.1021/es3037862, 2013.

Baker, K. R., Woody, M. C., Valin, L., Szykman, J., Yates, E. L., Iraci, L. T., Choi, H. D., Soja, A. J., Koplitz, S. N., Zhou, 695 L., Campuzano-Jost, P., Jimenez, J. L., and Hair, J. W.: Photochemical model evaluation of 2013 California wild fire air quality impacts using surface, aircraft, and satellite data, Science of The Total Environment, 637–638, 1137–1149, https://doi.org/10.1016/j.scitotenv.2018.05.048, 2018.

Berasategui, M., Amedro, D., Vereecken, L., Lelieveld, J., and Crowley, J. N.: Reaction between CH₃C(O)OOH (peracetic acid) and OH in the gas phase: a combined experimental and theoretical study of the kinetics and mechanism, 20, 13541–13555, https://doi.org/10.5194/acp-20-13541-2020, 2020.

Box, G. E. P.: Science and Statistics, 71, 791–799, https://doi.org/10.2307/2286841, 1976.

Buysse, C. E., Kaulfus, A., Nair, U., and Jaffe, D. A.: Relationships between Particulate Matter, Ozone, and Nitrogen Oxides during Urban Smoke Events in the Western US, 53, 12519–12528, https://doi.org/10.1021/acs.est.9b05241, 2019.

Caravan, R. L., Khan, M. A. H., Zádor, J., Sheps, L., Antonov, I. O., Rotavera, B., Ramasesha, K., Au, K., Chen, M., Rösch, D., Osborn, D. L., Fittschen, C., Schoemaecker, C., Duncianu, M., Grira, A., Dusanter, S., Tomas, A., Percival, C. J., Shallcross, D. E., and Taatjes, C. A.: The reaction of hydroxyl and methylperoxy radicals is not a major source of atmospheric methanol, 9, 4343, https://doi.org/10.1038/s41467-018-06716-x, 2018.

Chai, J., Dibb, J. E., Anderson, B. E., Bekker, C., Blum, D. E., Heim, E., Jordan, C. E., Joyce, E. E., Kaspari, J. H., Munro, H., Walters, W. W., and Hastings, M. G.: Isotopic constraints on wildfire derived HONO, 1–39, https://doi.org/10.5194/acp-2021-225, 2021.

Coggon, M. M., Lim, C. Y., Koss, A. R., Sekimoto, K., Yuan, B., Gilman, J. B., Hagan, D. H., Selimovic, V., Zarzana, K. J., Brown, S. S., M Roberts, J., Müller, M., Yokelson, R., Wisthaler, A., Krechmer, J. E., Jimenez, J. L., Cappa, C., Kroll, J. H., De Gouw, J., and Warneke, C.: OH chemistry of non-methane organic gases (NMOGs) emitted from laboratory and ambient biomass burning smoke: Evaluating the influence of furans and oxygenated aromatics on ozone and secondary NMOG formation, 19, 14875–14899, https://doi.org/10.5194/acp-19-14875-2019, 2019.

Daranlot, J., Hickson, K. M., Loison, J.-C., Méreau, R., Caralp, F., Forst, W., and Bergeat, A.: Gas-Phase Kinetics of the Hydroxyl Radical Reaction with Allene: Absolute Rate Measurements at Low Temperature, Product Determinations, and Calculations, J. Phys. Chem. A, 116, 10871–10881, https://doi.org/10.1021/jp304831x, 2012.

Day, D. A., Campuzano-Jost, P., Nault, B. A., Palm, B. B., Hu, W., Guo, H., Wooldridge, P. J., Cohen, R. C., Docherty, K. S., Huffman, J. A., de Sá, S. S., Martin, S. T., and Jimenez, J. L.: A Systematic Re-evaluation of Methods for Quantification of Bulk Particle-phase Organic Nitrates Using Real-time Aerosol Mass Spectrometry, 1–35, https://doi.org/10.5194/amt-2021-263, 2021.

Decker, Z. C. J., Zarzana, K. J., Coggon, M., Min, K.-E., Pollack, I., Ryerson, T. B., Peischl, J., Edwards, P., Dubé, W. P., Markovic, M. Z., Roberts, J. M., Veres, P. R., Graus, M., Warneke, C., de Gouw, J., Hatch, L. E., Barsanti, K. C., and Brown, S. S.: Nighttime Chemical Transformation in Biomass Burning Plumes: A Box Model Analysis Initialized with Aircraft Observations, 53, 2529–2538, https://doi.org/10.1021/acs.est.8b05359, 2019.

Decker, Z. C. J., Robinson, M. A., Barsanti, K. C., Bourgeois, I., Coggon, M. M., DiGangi, J. P., Diskin, G. S., Flocke, F. M., Franchin, A., Fredrickson, C. D., Hall, S. R., Halliday, H., Holmes, C. D., Huey, L. G., Lee, Y. R., Lindaas, J., Middlebrook, A. M., Montzka, D. D., Moore, R. H., Neuman, J. A., Nowak, J. B., Palm, B. B., Peischl, J., Rickly, P. S., Rollins, A. W., Ryerson, T. B., Schwantes, R. H., Thornhill, L., Thornton, J. A., Tyndall, G. S., Ullmann, K., Van Rooy, P., Veres, P. R., Weinheimer, A. J., Wiggins, E., Winstead, E., Womack, C., and Brown, S. S.: Nighttime and Daytime Dark Oxidation Chemistry in Wildfire Plumes: An Observation and Model Analysis of FIREX-AQ Aircraft Data, 1–45, https://doi.org/10.5194/acp-2021-267, 2021.

Duncan, B. N., Logan, J. A., Bey, I., Megretskaia, I. A., Yantosca, R. M., Novelli, P. C., Jones, N. B., and Rinsland, C. P.: Global budget of CO, 1988–1997: Source estimates and validation with a global model, 112, https://doi.org/10.1029/2007JD008459, 2007.

Forrister, H., Liu, J., Scheuer, E., Dibb, J., Ziemba, L., Thornhill, K. L., Anderson, B., Diskin, G., Perring, A. E., Schwarz, J. P., Campuzano-Jost, P., Day, D. A., Palm, B. B., Jimenez, J. L., Nenes, A., and Weber, R. J.: Evolution of brown carbon in wildfire plumes, 42, 4623–4630, https://doi.org/10.1002/2015GL063897, 2015.

740 Gilman, J. B., Lerner, B. M., Kuster, W. C., Goldan, P. D., Warneke, C., Veres, P. R., Roberts, J. M., de Gouw, J. A., Burling, I. R., and Yokelson, R. J.: Biomass burning emissions and potential air quality impacts of volatile organic compounds and other trace gases from temperate fuels common in the US, 15, 13915–13938, https://doi.org/10.5194/acp-15-13915-2015, 2015.

Gustafson, W. and Yu, S.: Generalized approach for using unbiased symmetric metrics with negative values: normalized mean
745 bias factor and normalized mean absolute error factor, 13, 262–267, https://doi.org/10.1002/asl.393, 2012.

Hatch, L. E., Yokelson, R. J., Stockwell, C. E., Veres, P. R., Simpson, I. J., Blake, D. R., Orlando, J. J., and Barsanti, K. C.: Multi-instrument comparison and compilation of non-methane organic gas emissions from biomass burning and implications for smoke-derived secondary aerosol precursors, 17, 1471–1489, https://doi.org/10.5194/acp-17-1471-2017, 2017.

Hatch, L. E., Jen, C. N., Kreisberg, N. M., Selimovic, V., Yokelson, R. J., Stamatis, C., York, R. A., Foster, D., Stephens, S.
750 L., Goldstein, A. H., and Barsanti, K. C.: Highly Speciated Measurements of Terpenoids Emitted from Laboratory and Mixed-Conifer Forest Prescribed Fires, 53, 9418–9428, https://doi.org/10.1021/acs.est.9b02612, 2019.

Heald, C. L. and Kroll, J. H.: The fuel of atmospheric chemistry: Toward a complete description of reactive organic carbon, 6, eaay8967, https://doi.org/10.1126/sciadv.aay8967, 2020.

Hodshire, A. L., Akherati, A., Alvarado, M. J., Brown-Steiner, B., Jathar, S. H., Jimenez, J. L., Kreidenweis, S. M., Lonsdale,
755 C. R., Onasch, T. B., Ortega, A. M., and Pierce, J. R.: Aging Effects on Biomass Burning Aerosol Mass and Composition: A Critical Review of Field and Laboratory Studies, Environ. Sci. Technol., 53, 10007–10022, https://doi.org/10.1021/acs.est.9b02588, 2019.

Jaffe, D. A. and Wigder, N. L.: Ozone production from wildfires: A critical review, 51, 1–10, https://doi.org/10.1016/j.atmosenv.2011.11.063, 2012.

760 Jenkin, M. E., Saunders, S. M., and Pilling, M. J.: The tropospheric degradation of volatile organic compounds: A protocol for mechanism development, 31, 81–104, 1997.

Jenkin, M. E., Young, J. C., and Rickard, A. R.: The MCM v3.3.1 degradation scheme for isoprene, 15, 11433–11459, https://doi.org/10.5194/acp-15-11433-2015, 2015.

Jenkin, M. E., Valorso, R., Aumont, B., and Rickard, A. R.: Estimation of rate coefficients and branching ratios for reactions
765 of organic peroxy radicals for use in automated mechanism construction, 19, 7691–7717, https://doi.org/10.5194/acp-19-7691-2019, 2019.

Juncosa Calahorrano, J. F. J., Lindaas, J., O'Dell, K., Palm, B. B., Peng, Q., Flocke, F., Pollack, I. B., Garofalo, L. A., Farmer, D. K., Pierce, J. R., Collett, J. L., Weinheimer, A., Campos, T., Hornbrook, R. S., Hall, S. R., Ullmann, K., Pothier, M. A., Apel, E. C., Permar, W., Hu, L., Hills, A. J., Montzka, D., Tyndall, G., Thornton, J. A., and Fischer, E. V.: Daytime Oxidized
770 Reactive Nitrogen Partitioning in Western U.S. Wildfire Smoke Plumes, 126, e2020JD033484, https://doi.org/10.1029/2020JD033484, 2020.

Kelp, M. M., Jacob, D. J., Kutz, J. N., Marshall, J. D., and Tessum, C. W.: Toward Stable, General Machine-Learned Models of the Atmospheric Chemical System, 125, e2020JD032759, https://doi.org/10.1029/2020JD032759, 2020.

Kleinman, L. I.: The dependence of tropospheric ozone production rate on ozone precursors, Atmospheric Environment, 39,
575–586, https://doi.org/10.1016/j.atmosenv.2004.08.047, 2005.

Kleinman, L. I., Daum, P. H., Lee, J. H., Lee, Y.-N., Nunnermacker, L. J., Springston, S. R., Newman, L., Weinstein-Lloyd, J., and Sillman, S.: Dependence of ozone production on NO and hydrocarbons in the troposphere, 24, 2299–2302, https://doi.org/10.1029/97GL02279, 1997.

Koss, A. R., Sekimoto, K., Gilman, J. B., Selimovic, V., Coggon, M. M., Zarzana, K. J., Yuan, B., Lerner, B. M., Brown, S. S., Jimenez, J. L., Krechmer, J., Roberts, J. M., Warneke, C., Yokelson, R. J., and de Gouw, J.: Non-methane organic gas emissions from biomass burning: identification, quantification, and emission factors from PTR-ToF during the FIREX 2016 laboratory experiment, 18, 3299–3319, https://doi.org/10.5194/acp-18-3299-2018, 2018.

Lee, M., Heikes, B. G., Jacob, D. J., Sachse, G., and Anderson, B.: Hydrogen peroxide, organic hydroperoxide, and formaldehyde as primary pollutants from biomass burning, 102, 1301–1309, https://doi.org/10.1029/96JD01709, 1997.

Liao, J., Wolfe, G. M., Hannun, R. A., St. Clair, J. M., Hanisco, T. F., Gilman, J. B., Lamplugh, A., Selimovic, V., Diskin, G. S., Nowak, J. B., Halliday, H. S., DiGangi, J. P., Hall, S. R., Ullmann, K., Holmes, C. D., Fite, C. H., Agastra, A., Ryerson, T. B., Peischl, J., Bourgeois, I., Warneke, C., Coggon, M. M., Gkatzelis, G. I., Sekimoto, K., Fried, A., Richter, D., Weibring, P., Apel, E. C., Hornbrook, R. S., Brown, S. S., Womack, C. C., Robinson, M. A., Washenfelder, R. A., Veres, P. R., and Neuman, J. A.: Formaldehyde evolution in U.S. wildfire plumes during FIREX-AQ, 1–38, https://doi.org/10.5194/acp-2021-389, 2021.

Lindaas, J., Pollack, I. B., Garofalo, L. A., Pothier, M. A., Farmer, D. K., Kreidenweis, S. M., Campos, T. L., Flocke, F., Weinheimer, A. J., Montzka, D. D., Tyndall, G. S., Palm, B. B., Peng, Q., Thornton, J. A., Permar, W., Wielgasz, C., Hu, L., Ottmar, R. D., Restaino, J. C., Hudak, A. T., Ku, I.-T., Zhou, Y., Sive, B. C., Sullivan, A., Collett, J. L., and Fischer, E. V.: Emissions of Reactive Nitrogen from Western U.S. Wildfires during Summer 2018, n/a, e2020JD032657, https://doi.org/10.1029/2020JD032657, 2020.

Lindaas, J., Pollack, I. B., Calahorrano, J. J., O'Dell, K., Garofalo, L. A., Pothier, M. A., Farmer, D. K., Kreidenweis, S. M., Campos, T., Flocke, F., Weinheimer, A. J., Montzka, D. D., Tyndall, G. S., Apel, E. C., Hills, A. J., Hornbrook, R. S., Palm, B. B., Peng, Q., Thornton, J. A., Permar, W., Wielgasz, C., Hu, L., Pierce, J. R., Collett, J. L., Sullivan, A. P., and Fischer, E. V.: Empirical Insights Into the Fate of Ammonia in Western U.S. Wildfire Smoke Plumes, 126, e2020JD033730, https://doi.org/10.1029/2020JD033730, 2021.

Liu, X., Zhang, Y., Huey, L. G., Yokelson, R. J., Wang, Y., Jimenez, J. L., Campuzano-Jost, P., Beyersdorf, A. J., Blake, D. R., Choi, Y., St. Clair, J. M., Crounse, J. D., Day, D. A., Diskin, G. S., ried, A., Hall, S. R., Hanisco, T. F., King, L. E., Meinardi, S., Mikoviny, T., Palm, B. B., Peischl, J., Perring, A. E., Pollack, I. B., Ryerson, T. B., Sachse, G., Schwarz, J. P., Simpson, I. J., Tanner, D. J., Thornhil, K. L., Ullmann, K., Weber, R. J., Wennberg, P. O., Wisthaler, A., Wolfe, G. M., and Ziemba, L. D.: Agricultural fires in the southeastern U.S. during SEAC4RS: Emissions of trace gases and particles and evolution of ozone, reactive nitrogen, and organic aerosol, 121, 7383–7414, https://doi.org/10.1002/2016JD025040, 2016.

Liu, X., Huey, L. G., Yokelson, R. J., Selimovic, V., Simpson, I. J., Müller, M., Jimenez, J. L., Campuzano-Jost, P., Beyersdorf, A. J., Blake, D. R., Butterfield, Z., Choi, Y., Crounse, J. D., Day, D. A., Diskin, G. S., Dubey, M. K., Fortner, E., Hanisco, T. F., Hu, W., King, L. E., Kleinman, L., Meinardi, S., Mikoviny, T., Onasch, T. B., Palm, B. B., Peischl, J., Pollack, I. B., Ryerson, T. B., Sachse, G. W., Sedlacek, A. J., Shilling, J. E., Springston, S., St. Clair, J. M., Tanner, D. J., Teng, A. P., Wennberg, P. O., Wisthaler, A., and Wolfe, G. M.: Airborne measurements of western U.S. wildfire emissions: Comparison with prescribed burning and air quality implications, n/a-n/a, https://doi.org/10.1002/2016JD026315, 2017.

Lonsdale, C., Alvarado, M., Hodshire, A., Ramnarine, E., and Pierce, J.: Simulating Forest Fire Plume Dispersion, Chemistry, and Aerosol Formation Using SAM-ASP version 1.0, 1–19, https://doi.org/10.5194/gmd-2019-221, 2019.

Lydersen, J. M., North, M. P., and Collins, B. M.: Severity of an uncharacteristically large wildfire, the Rim Fire, in forests
815 with relatively restored frequent fire regimes, 328, 326–334, https://doi.org/10.1016/j.foreco.2014.06.005, 2014.

Ma, Q., Zhong, C., Ma, J., Ye, C., Zhao, Y., Liu, Y., Zhang, P., Chen, T., Liu, C., Chu, B., and He, H.: Comprehensive Study
about the Photolysis of Nitrates on Mineral Oxides, Environ. Sci. Technol., 55, 8604–8612,
https://doi.org/10.1021/acs.est.1c02182, 2021.

Mason, S. A., Field, R. J., Yokelson, R. J., Kochivar, M. A., Tinsley, M. R., Ward, D. E., and Hao, W. M.: Complex effects
820 arising in smoke plume simulations due to inclusion of direct emissions of oxygenated organic species from biomass
combustion, 106, 12527–12539, https://doi.org/10.1029/2001jd900003, 2001.

Mauzerall, D. L., Logan, J. A., Jacob, D. J., Anderson, B. E., Blake, D. R., Bradshaw, J. D., Heikes, B., Sachse, G. W., Singh,
H., Talbot, B., Mauzerall, L., Logan, A., Jacob, J., Blake, R., Bradshaw, D., and Sachse, W.: Photochemistry in biomass
burning plumes and implications for tropospheric ozone over the tropical South Atlantic, 103, 8401–8423,
825 https://doi.org/10.1029/97jd02612, 1998.

McClure, C. D. and Jaffe, D. A.: US particulate matter air quality improves except in wildfire-prone areas, 115, 7901–7906,
https://doi.org/10.1073/pnas.1804353115, 2018.

Müller, M., Anderson, B. E., Beyersdorf, A. J., Crawford, J. H., Diskin, G. S., Eichler, P., Fried, A., Keutsch, F. N., Mikoviny,
T., Thornhill, K. L., Walega, J. G., Weinheimer, A. J., Yang, M., Yokelson, R. J., and Wisthaler, A.: In situ measurements and
830 modeling of reactive trace gases in a small biomass burning plume, 16, 3813–3824, https://doi.org/10.5194/acp-16-3813-2016,
2016.

Palm, B. B., Peng, Q., Fredrickson, C. D., Lee, B. H., Garofalo, L. A., Pothier, M. A., Kreidenweis, S. M., Farmer, D. K.,
Pokhrel, R. P., Shen, Y., Murphy, S. M., Permar, W., Hu, L., Campos, T. L., Hall, S. R., Ullmann, K., Zhang, X., Flocke, F.,
Fischer, E. V., and Thornton, J. A.: Quantification of organic aerosol and brown carbon evolution in fresh wildfire plumes,
835 PNAS, 117, 29469–29477, https://doi.org/10.1073/pnas.2012218117, 2020.

Peng, Q., Palm, B. B., Melander, K. E., Lee, B. H., Hall, S. R., Ullmann, K., Campos, T., Weinheimer, A. J., Apel, E. C.,
Hornbrook, R. S., Hills, A. J., Montzka, D. D., Flocke, F., Hu, L., Permar, W., Wielgasz, C., Lindaas, J., Pollack, I. B., Fischer,
E. V., Bertram, T. H., and Thornton, J. A.: HONO Emissions from Western U.S. Wildfires Provide Dominant Radical Source
in Fresh Wild fi re Smoke, https://doi.org/10.1021/acs.est.0c00126, 2020.

840 Permar, W., Wang, Q., Selimovic, V., Wielgasz, C., Yokelson, R. J., Hornbrook, R. S., Hills, A. J., Apel, E. C., Ku, I.-T.,
Zhou, Y., Sive, B. C., Sullivan, A. P., Collett, J. L., Campos, T. L., Palm, B. B., Peng, Q., Thornton, J. A., Garofalo, L. A.,
Farmer, D. K., Kreidenweis, S. M., Levin, E. J. T., DeMott, P. J., Flocke, F., Fischer, E. V., and Hu, L.: Emissions of trace
organic gases from western U.S. wildfires based on WE-CAN aircraft measurements, e2020JD033838,
https://doi.org/10.1029/2020JD033838, 2021.

845 Perring, A. E., Schwarz, J. P., Markovic, M. Z., Fahey, D. W., Jimenez, J. L., Campuzano-Jost, P., Palm, B. D., Wisthaler, A.,
Mikoviny, T., Diskin, G., Sachse, G., Ziemba, L., Anderson, B., Shingler, T., Crosbie, E., Sorooshian, A., Yokelson, R., and
Gao, R.-S.: In situ measurements of water uptake by black carbon-containing aerosol in wildfire plumes, 122, 1086–1097,
https://doi.org/10.1002/2016JD025688, 2017.

Peterson, D. A., Hyer, E. J., Campbell, J. R., Fromm, M. D., Hair, J. W., Butler, C. F., and Fenn, M. A.: The 2013 Rim Fire:
850 Implications for Predicting Extreme Fire Spread, Pyroconvection, and Smoke Emissions, 96, 229–247,
https://doi.org/10.1175/bams-d-14-00060.1, 2015.

Roberts, J. M., Stockwell, C. E., Yokelson, R. J., de Gouw, J., Liu, Y., Selimovic, V., Koss, A. R., Sekimoto, K., Coggon, M. M., Yuan, B., Zarzana, K. J., Brown, S. S., Santin, C., Doerr, S. H., and Warneke, C.: The nitrogen budget of laboratory-simulated western US wildfires during the FIREX 2016 Fire Lab study, 20, 8807–8826, https://doi.org/10.5194/acp-20-8807-2020, 2020.

Robinson, M. A., Decker, Z. C. J., Barsanti, K. C., Coggon, M. M., Flocke, F. M., Franchin, A., Fredrickson, C. D., Gilman, J. B., Gkatzelis, G. I., Holmes, C. D., Lamplugh, A., Lavi, A., Middlebrook, A. M., Montzka, D. M., Palm, B. B., Peischl, J., Pierce, B., Schwantes, R. H., Sekimoto, K., Selimovic, V., Tyndall, G. S., Thornton, J. A., Van Rooy, P., Warneke, C., Weinheimer, A. J., and Brown, S. S.: Variability and Time of Day Dependence of Ozone Photochemistry in Western Wildfire Plumes, Environ. Sci. Technol., 55, 10280–10290, https://doi.org/10.1021/acs.est.1c01963, 2021.

Romer, P. S., Wooldridge, P. J., Crounse, J. D., Kim, M. J., Wennberg, P. O., Dibb, J. E., Scheuer, E., Blake, D. R., Meinardi, S., Brosius, A. L., Thames, A. B., Miller, D. O., Brune, W. H., Hall, S. R., Ryerson, T. B., and Cohen, R. C.: Constraints on Aerosol Nitrate Photolysis as a Potential Source of HONO and NOx, 52, 13738–13746, https://doi.org/10.1021/acs.est.8b03861, 2018.

Saide, P. E., Peterson, D. A., da Silva, A., Anderson, B., Ziemba, L. D., Diskin, G., Sachse, G., Hair, J., Butler, C., Fenn, M., Jimenez, J. L., Campuzano-Jost, P., Perring, A. E., Schwarz, J. P., Markovic, M. Z., Russell, P., Redemann, J., Shinozuka, Y., Streets, D. G., Yan, F., Dibb, J., Yokelson, R., Toon, O. B., Hyer, E., and Carmichael, G. R.: Revealing important nocturnal and day-to-day variations in fire smoke emissions through a multiplatform inversion, 42, 3609–3618, https://doi.org/10.1002/2015gl063737, 2015.

Sangwan, M. and Zhu, L.: Absorption Cross Sections of 2-Nitrophenol in the 295–400 nm Region and Photolysis of 2-Nitrophenol at 308 and 351 nm, J. Phys. Chem. A, 120, 9958–9967, https://doi.org/10.1021/acs.jpca.6b08961, 2016.

Saunders, S. M., Jenkin, M. E., Derwent, R. G., and Pilling, M. J.: Protocol for the development of the Master Chemical Mechanism, MCM v3 (Part A): tropospheric degradation of non-aromatic volatile organic compounds, 3, 161–180, 2003.

Schroeder, J. R., Crawford, J. H., Fried, A., Walega, J., Weinheimer, A., Wisthaler, A., Müller, M., Mikoviny, T., Chen, G., Shook, M., Blake, D. R., and Tonnesen, G. S.: New insights into the column CH2O/NO2 ratio as an indicator of near-surface ozone sensitivity, 122, 8885–8907, https://doi.org/doi:10.1002/2017JD026781, 2017.

Sekimoto, K., Koss, A. R., Gilman, J. B., Selimovic, V., Coggon, M. M., Zarzana, K. J., Yuan, B., Lerner, B. M., Brown, S. S., Warneke, C., Yokelson, R. J., Roberts, J. M., and de Gouw, J.: High- and low-temperature pyrolysis profiles describe volatile organic compound emissions from western US wildfire fuels, 1–39, https://doi.org/10.5194/acp-2018-52, 2018.

Shi, Q., Tao, Y., Krechmer, J. E., Heald, C. L., Murphy, J. G., Kroll, J. H., and Ye, Q.: Laboratory Investigation of Renoxification from the Photolysis of Inorganic Particulate Nitrate, Environ. Sci. Technol., 55, 854–861, https://doi.org/10.1021/acs.est.0c06049, 2021.

Stein, A. F., Draxler, R. R., Rolph, G. D., Stunder, B. J. B., Cohen, M. D., and Ngan, F.: NOAA's HYSPLIT Atmospheric Transport and Dispersion Modeling System, 96, 2059–2077, https://doi.org/10.1175/BAMS-D-14-00110.1, 2015.

Stemmler, K., Ammann, M., Donders, C., Kleffmann, J., and George, C.: Photosensitized reduction of nitrogen dioxide on humic acid as a source of nitrous acid, 440, 195–198, https://doi.org/10.1038/nature04603, 2006.

Theys, N., Volkamer, R., Müller, J.-F., Zarzana, K. J., Kille, N., Clarisse, L., De Smedt, I., Lerot, C., Finkenzeller, H., Hendrick, F., Koenig, T. K., Lee, C. F., Knote, C., Yu, H., and Van Roozendael, M.: Global nitrous acid emissions and levels of regional oxidants enhanced by wildfires, 13, 681–686, https://doi.org/10.1038/s41561-020-0637-7, 2020.

890   Toon, O. B., Maring, H., Dibb, J., Ferrare, R., Jacob, D. J., Jensen, E. J., Luo, Z. J., Mace, G. G., Pan, L. L., Pfister, L., Rosenlof, K. H., Redemann, J., Reid, J. S., Singh, H. B., Thompson, A. M., Yokelson, R., Minnis, P., Chen, G., Jucks, K. W., and Pszenny, A.: Planning, implementation, and scientific goals of the Studies of Emissions and Atmospheric Composition, Clouds and Climate Coupling by Regional Surveys (SEAC(4)RS) field mission, 121, 4967–5009, https://doi.org/10.1002/2015JD024297, 2016.

895   Ulbrich, I. M., Canagaratna, M. R., Zhang, Q., Worsnop, D. R., and Jimenez, J. L.: Interpretation of organic components from Positive Matrix Factorization of aerosol mass spectrometric data, 9, 2891–2918, https://doi.org/10.5194/acp-9-2891-2009, 2009.

Val Martin, M., Heald, C. L., Lamarque, J. F., Tilmes, S., Emmons, L. K., and Schichtel, B. A.: How emissions, climate, and land use change will impact mid-century air quality over the United States: A focus on effects at national parks, 15, 2805–
900   2823, https://doi.org/10.5194/acp-15-2805-2015, 2015.

Wang, S., Coggon, M. M., Gkatzelis, G. I., Warneke, C., Bourgeois, I., Ryerson, T., Peischl, J., Veres, P. R., Neuman, J. A., Hair, J., Shingler, T., Fenn, M., Diskin, G., Huey, L. G., Lee, Y. R., Apel, E. C., Hornbrook, R. S., Hills, A. J., Hall, S. R., Ullmann, K., Bela, M. M., Trainer, M. K., Kumar, R., Orlando, J. J., Flocke, F. M., and Emmons, L. K.: Chemical Tomography in a Fresh Wildland Fire Plume: A Large Eddy Simulation (LES) Study, 126, e2021JD035203,
905   https://doi.org/10.1029/2021JD035203, 2021.

Wiedinmyer, C., Akagi, S. K., Yokelson, R. J., Emmons, L. K., Al-Saadi, J. A., Orlando, J. J., and Soja, A. J.: The Fire INventory from NCAR (FINN): a high resolution global model to estimate the emissions from open burning, 4, 625–641, https://doi.org/10.5194/gmd-4-625-2011, 2011.

Wiggins, E. B., Soja, A. J., Gargulinski, E., Halliday, H. S., Pierce, R. B., Schmidt, C. C., Nowak, J. B., DiGangi, J. P., Diskin,
910   G. S., Katich, J. M., Perring, A. E., Schwarz, J. P., Anderson, B. E., Chen, G., Crosbie, E. C., Jordan, C., Robinson, C. E., Sanchez, K. J., Shingler, T. J., Shook, M., Thornhill, K. L., Winstead, E. L., Ziemba, L. D., and Moore, R. H.: High Temporal Resolution Satellite Observations of Fire Radiative Power Reveal Link Between Fire Behavior and Aerosol and Gas Emissions, 47, e2020GL090707, https://doi.org/10.1029/2020GL090707, 2020.

Wolfe, G. M., Marvin, M. M., Roberts, S. J., Travis, K. R., and Liao, J.: The Framework for 0-D Atmospheric Modeling
915   (F0AM) v3.1, 9, 3309–3319, https://doi.org/10.5194/gmd-9-3309-2016, 2016.

Wooldridge, P. J., Perring, A. E., Bertram, T. H., Flocke, F. M., Roberts, J. M., Singh, H. B., Huey, L. G., Thornton, J. A., Wolfe, G. M., Murphy, J. G., Fry, J. L., Rollins, A. W., LaFranchi, B. W., and Cohen, R. C.: Total peroxy nitrates (SPNs) in the atmosphere: the thermal dissociation-laser induced fluorescence (TD-LIF) technique and comparisons to speciated PAN measurements, 3, 593–607, https://doi.org/10.5194/amt-3-593-2010, 2010.

920   Xu, B., Garrec, J., Nicolle, A., Matrat, M., and Catoire, L.: Temperature and Pressure Dependent Rate Coefficients for the Reaction of Ketene with Hydroxyl Radical, J. Phys. Chem. A, 123, 2483–2496, https://doi.org/10.1021/acs.jpca.8b11273, 2019.

Yates, E. L., Iraci, L. T., Singh, H. B., Tanaka, T., Roby, M. C., Hamill, P., Clements, C. B., Lareau, N., Contezac, J., Blake, D. R., Simpson, I. J., Wisthaler, A., Mikoviny, T., Diskin, G. S., Beyersdorf, A. J., Choi, Y., Ryerson, T. B., Jimenez, J. L.,
925   Campuzano-Jost, P., Loewenstein, M., and Gore, W.: Airborne measurements and emission estimates of greenhouse gases and other trace constituents from the 2013 California Yosemite Rim wildfire, 127, 293–302, https://doi.org/10.1016/j.atmosenv.2015.12.038, 2016.

Ye, C., Zhang, N., Gao, H., and Zhou, X.: Photolysis of Particulate Nitrate as a Source of HONO and NOx, Environ. Sci. Technol., 51, 6849–6856, https://doi.org/10.1021/acs.est.7b00387, 2017.

930   Ye, C., Zhou, X., Pu, D., Stutz, J., Festa, J., Spolaor, M., Tsai, C., Cantrell, C., Mauldin III, R. L., Weinheimer, A., Hornbrook, R. S., Apel, E. C., Guenther, A., Kaser, L., Yuan, B., Karl, T., Haggerty, J., Hall, S., Ullmann, K., Smith, J., and Ortega, J.: Tropospheric HONO distribution and chemistry in the southeastern US, 18, 9107–9120, https://doi.org/10.5194/acp-18-9107-2018, 2018.

Yokelson, R. J., Christian, T. J., Karl, T. G., and Guenther, A.: The tropical forest and fire emissions experiment: laboratory
935   fire measurements and synthesis of campaign data, 8, 3509–3527, 2008.

Yokelson, R. J., Burling, I. R., Gilman, J. B., Warneke, C., Stockwell, C. E., de Gouw, J., Akagi, S. K., Urbanski, S. P., Veres, P., Roberts, J. M., Kuster, W. C., Reardon, J., Griffith, D. W. T., Johnson, T. J., Hosseini, S., Miller, J. W., Cocker III, D. R., Jung, H., and Weise, D. R.: Coupling field and laboratory measurements to estimate the emission factors of identified and unidentified trace gases for prescribed fires, 13, 89–116, https://doi.org/10.5194/acp-13-89-2013, 2013.

940   Yu, P., Toon, O. B., Bardeen, C. G., Bucholtz, A., Rosenlof, K. H., Saide, P. E., Da Silva, A., Ziemba, L. D., Thornhill, K. L., Jimenez, J.-L., Campuzano-Jost, P., Schwarz, J. P., Perring, A. E., Froyd, K. D., Wagner, N. L., Mills, M. J., and Reid, J. S.: Surface dimming by the 2013 Rim Fire simulated by a sectional aerosol model, 121, 7079–7087, https://doi.org/10.1002/2015JD024702, 2016a.

Yu, P., Toon, O. B., Bardeen, C. G., Bucholtz, A., Rosenlof, K. H., Saide, P. E., Da Silva, A., Ziemba, L. D., Thornhill, K. L.,
945   Jimenez, J.-L., Campuzano-Jost, P., Schwarz, J. P., Perring, A. E., Froyd, K. D., Wagner, N. L., Mills, M. J., and Reid, J. S.: Surface dimming by the 2013 Rim Fire simulated by a sectional aerosol model, 121, 7079–7087, https://doi.org/10.1002/2015JD024702, 2016b.

Zhang, J., An, J., Qu, Y., Liu, X., and Chen, Y.: Impacts of potential HONO sources on the concentrations of oxidants and secondary organic aerosols in the Beijing-Tianjin-Hebei region of China, Science of The Total Environment, 647, 836–852,
950   https://doi.org/10.1016/j.scitotenv.2018.08.030, 2019.